MilliporeSigma

Material Matters™

VOLUME 12 • NUMBER 1

Nanomaterial Synthesis

Creativity at the Nanoscale

Methods of **SYNTHESIZING MONODISPERSE COLLOIDAL QUANTUM DOTS**

NANOWIRE SYNTHESIS: From Top-Down to Bottom-Up

BUILDING AND ENGINEERING Micro/Nano Architectures of Single-Walled Carbon Nanotubes for Electronic Applications

SYNTHESIS OF GOLD NANORODS: Avoiding Common Pitfalls

The life science business of Merck KGaA, Darmstadt, Germany operates as MilliporeSigma in the U.S. and Canada.

Material Matters™
VOL. 12 • NO. 1

Introduction

Taryn L. Fuhrman-Hall, M.B.A.
Product Manager,
Materials Science

Welcome to the first issue of *Material Matters*™ for 2017, featuring methods for the synthesis of nanomaterials. Nanomaterials have been a focus of materials research for many years, but recent advances have accelerated their adoption in the electronics, energy, and biomedical industries. These advances have increased the need for scalable and reproducible nanomaterials synthesis allowing for high levels of control of size, shape and functionality. We are also pleased to use this issue to introduce our updated branding and design theme, highlighted by our new name, MilliporeSigma. See below for more information on this exciting transformation.

In the first article, Professor Osman M. Bakr (King Abdullah University of Science and Technology, Saudi Arabia) summarizes methods used in his laboratory to synthesize colloidal quantum dots (CQDs), specifically monodisperse cadmium- and lead-based CQDs. Applications of these novel materials have grown rapidly in recent years due to their exceptional efficiency.

The unique properties of nanowires have generated great interest among both fundamental researchers and developers of new optical and electronic devices. In the second article from Professor James F. Cahoon (University of North Carolina at Chapel Hill, USA), reliable and controllable nanowire synthesis methods of both top-down fabrication and bottom-up synthesis are explored.

Carbon nanotubes are now established as an important building block of nanotechnology, yet challenges remain in creating scalable and reproducible materials. Professor Yung Joon Jung (Northeastern University, USA) presents a specific method for fabricating highly organized and controlled micro- and nanoscale single walled carbon nanotubes on various substrates.

Gold nanoparticles are an indispensable component in common diagnostics and drug delivery products used globally. Gold nanorods represent present additional functionalities because of their unique anisotropic shape and resulting optical adsorption properties. In the fourth article, Dr. Kimberly A. Homan (NanoHybrids Inc., USA) discusses seed-mediated gold nanorod synthesis and presents common synthesis pitfalls and how to avoid them.

Each article in this publication is accompanied by a list of relevant materials available from MilliporeSigma Materials Science. For additional product information, visit us at **SigmaAldrich.com/matsci**. As always, please bother us with your new product suggestions as well as thoughts and comments for *Material Matters*™ at **matsci@sial.com**.

Welcome to the Future of *Material Matters*™

Bryce P. Nelson, Ph.D.
Materials Science
Initiative Lead

We are proud to use this issue introduce you to MilliporeSigma. The addition of Sigma-Aldrich to the MilliporeSigma family allows us to grow as a company and better serve our customers. We are confident that you will find the fundamental quality and trust that makes Aldrich and Sigma-Aldrich an essential part of laboratories worldwide remains intact. We continue to bring you the latest ideas and products to help drive your research on **SigmaAldrich.com**; previous issues of *Material Matters*™ are available online at **SigmaAldrich.com/mm**.

The transformation of our company and of our brand naturally drives an evolution in the design of *Material Matters*™, and we are excited to welcome you to a whole new look. Over its twelve-year history, *Material Matters*™ has consistently brought you reviews of the latest in materials science as well as information on new products for research. This new look is a reflection of the vibrant energy and passion that is driving science and technology today.

About the Cover

Innovative materials start with innovative chemistry. Our cover art highlights the importance of starting materials in the synthesis process, whether they be quantum dots, nanowires, gold nanorods, or engineered carbon nanotube architectures for novel electronic applications.

Merck KGaA, Darmstadt, Germany
Frankfurter Strasse 250
64293 Darmstadt, Germany
Phone +49 6151 72 0

To Place Orders / Customer Service
Contact your local office or visit
SigmaAldrich.com/order

Technical Service
Contact your local office or visit
SigmaAldrich.com/techinfo

General Correspondence
Materials Science
materialsscience@sial.com

Subscriptions
Request your FREE subscription to *Material Matters*™ at **SigmaAldrich.com/mm**

The entire *Material Matters*™ archive is available at **SigmaAldrich.com/mm**

Material Matters™ (ISSN 1933-9631) is a publication of Merck KGaA, Darmstadt, Germany

Table of Contents

Articles

Featured Products

Your Material Matters

Josef Zihlmann, Ph.D.
Head, Lab and Specialty Chemicals
Research Solutions Strategic Marketing & Innovation
MilliporeSigma

We welcome fresh product ideas. Do you have a material or compound you wish to see featured in our Materials Science line? If it is needed to accelerate your research, it matters. Send your suggestion to ***matsci@sial.com*** *for consideration.*

Dr. Anton Köck of the Materials Center Leoben Forschung GmbH (Austria) recommended the addition of CdSe/CdS core-shell type quantum rods (**900511**, **900512**, **900515**, and **900415**) to our catalog. The elongated structure of CdSe/CdS rods increases their photo and thermal stability. The quantum rods also possess high extinction coefficient and quantum yield which enhance their brightness by an order of magnitude compared to quantum dots.[1,2] These outstanding properties make the CdSe/CdS quantum rods promising for future use in displays, solid state lighting (LED) and lasers.

References

(1) Dimitrijevic, J.; et al. *Nanoscale*. **2014**, *6*(17), 10413–10422.
(2) Zavelani-Rossi, M.; et al. *Nanoscale*. **2010**, *2*(6), 931–935.

CdSe/CdS core-shell type quantum rods, 5 mg/ml in hexane

Elongated quantum dots; QDs; Quantum rods; Fluorescent nanocrystals; CANdot® dispersion

fluorescence λ_{em} 530 nm	
900511-1ML	1 mL
fluorescence λ_{em} 560 nm	
900512-1ML	1 mL
fluorescence λ_{em} 590 nm	
900515-1ML	1 mL
fluorescence λ_{em} 620 nm	
900514-1ML	1 mL

Beyond pure

Ultra-high purity metals, salts, and oxides are essential in creating advanced materials. Explore the breadth of our portfolio's materials with purity of 99.999% or higher for applications such as:

- Photovoltaics
- Phosphor materials
- Nanoparticle synthesis
- Magnetic memory
- Biomedical applications
- Electronic devices

Metals	
Tellurium, pieces, 99.999% trace metals basis	**204544**
Aluminum, wire, diam. 1.0 mm, 99.999% trace metals basis	**266558**
Gold, beads, 1-6 mm, 99.999% trace metals basis	**326542**
Copper, powder, 99.999% trace metals basis	**203122**
Zinc, foil, thickness 0.25 mm, 99.999% trace metals basis	**267619**
Indium, beads, diam. 2-5 mm, 99.999% trace metals basis	**264113**
Bismuth, pieces, 1-12 mm, 99.999% trace metals basis	**556130**
Copper, foil, thickness 1.0 mm, 99.999% trace metals basis	**266744**
Mercury, electronic grade, 99.9999% trace metals basis	**294594**
Germanium, chips, 99.999% trace metals basis	**203343**
Oxides	
Lead(II) oxide, 99.999% trace metals basis	**203610**
Antimony(III) oxide, 99.999% trace metals basis	**202649**
Iron(III) oxide, ≥99.995% trace metals basis	**529311**
Bismuth(III) oxide, powder, 99.999% trace metals basis	**202827**
Zinc oxide, 99.999% trace metals basis	**204951**
Germanium(IV) oxide, powder, 99.999% trace metals basis	**483001**
Holmium(III) oxide, powder, 99.999% trace metals basis	**229679**
Copper(II) oxide, 99.999% trace metals basis	**203130**
Selenium dioxide, 99.999% trace metals basis	**204315**
Nickel(II) oxide, ≥99.995% (Trace Metals Analysis)	**481793**
Salts	

Product Description	Prod. No.
Gold(III) chloride hydrate, 99.999% trace metals basis	**254169**
Ammonium acetate, 99.999% trace metals basis	**372331**
Aluminum chloride, anhydrous, powder, 99.999% trace metals basis	**563919**
Lead(II) iodide, 99.999% trace metals basis	**203602**
Zinc chloride, 99.999% trace metals basis	**229997**
Silver nitrate, 99.9999% trace metals basis	**204390**
Copper(I) iodide, 99.999% trace metals basis	**215554**
Nickel(II) nitrate hexahydrate, 99.999% trace metals basis	**203874**
Copper(I) bromide, 99.999% trace metals basis	**254185**
Sodium carbonate, anhydrous, powder, 99.999% trace metals basis	**451614**
Gallium(III) chloride, beads, anhydrous, ≥99.999% trace metals basis	**427128**
Indium(III) chloride, 99.999% trace metals basis	**203440**
Ammonium sulfate, 99.999% trace metals basis	**204501**
Cesium chloride, ≥99.999% trace metals basis	**203025**
Cobalt(II) nitrate hexahydrate, 99.999% trace metals basis	**203106**
Lanthanum(III) chloride heptahydrate, 99.999% trace metals basis	**203521**

For a complete list of ultra-high purity products, visit **SigmaAldrich.com/uhp**

Methods of Synthesizing Monodisperse Colloidal Quantum Dots


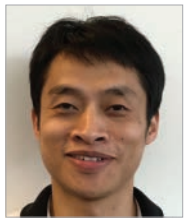


Lutfan Sinatra, Jun Pan, Osman M. Bakr*

Physical Science and Engineering Division
King Abdullah University of Science and Technology, Thuwal, Saudi Arabia
*Email: osman.bakr@kaust.edu.sa

Introduction

Colloidal quantum dots (CQDs) are semiconducting crystals of only a few nanometers (ca. 2–12 nm) coated with ligand/surfactant molecules to help prevent agglomeration. As CQDs exist on a nanometer scale, they can offer unique properties via quantum confinement.[1] It is possible to achieve highly tunable electrical and optical properties by adjusting the shape, size, and composition of a QD and in doing so, facilitate the use of QDs in a broad range of applications. QDs are particularly promising in optoelectronic devices such as light-emitting diodes, photovoltaics, photodetectors, lasers, and field-effect transistors.[2-4]

Since researchers first described the size-dependent properties of QDs at the beginning of the 1980s,[5] a variety of different QD nanocrystals have emerged,[6] and significant progress has been made in the realm of semiconductor particles, especially in terms of colloidal synthesis methods. The development of CQDs has been particularly promising in the area of solution-processable optoelectronic devices; for example, those involved in spin coating, ink-jet printing, blade coating, and screen printing have paved the way for the low-cost fabrication of large-area flexible devices.[7]

However, these developments have not been without their challenges. One particular challenge is in the synthesis of monodisperse and narrow size-distributed CQDs. Over the past 30 years, advances in the methods used to produce CQDs have resulted in the evolution of different approaches to synthesize them with uniform size. Monodisperse CQDs are significant because they possess relatively homogeneous properties that can be used in high-quality optoelectronic devices.

Herein we summarize a number of methods to synthesize CQDs, concentrating on the evolution of monodisperse cadmium- and lead-based CQDs—particularly CdSe, CdTe, PbS, and perovskite QDs—due to their wide-spread use and efficient properties. We discuss the various approaches for the batch synthesis of monodisperse QDs including hot-injection, heat-up, cluster-assisted, and microwave-assisted synthesis methods. We also assess continuous flow-assisted synthesis as a means of producing CQDs on a large production scale and compare the merits of the batch and continuous flow-assisted approaches.

The Hot-Injection Method

The current approaches to synthesizing monodisperse CQDs are predominantly based on the work of LaMer and Dinegar, who described how the production of monodisperse colloids is dependent on a rapid nucleation followed by the controlled growth of the existing nuclei (**Figure 1**).[8,9] Using this approach, Alivisatos and Bawendi et al. introduced the "hot-injection" method of synthesizing monodisperse CdS, CdSe, and CdTe QDs.[10,11] To this day, the hot-injection approach remains the most common method by which monodisperse nanocrystals are synthesized. It involves the production of homogeneous nuclei via the rapid injection of organometallic reagents into a hot solvent. The reaction solution used during this process also contains surfactant molecules/ligands to prevent QDs from agglomerating. The ligands that are typically employed include alkylphosphine and alkylphosphine oxides (e.g., trioctylphosphine, **Prod. No. 718165** and trioctylphosphine oxide, **Prod. No. 223301**), long-chain carboxylic acids (e.g., oleic acid, **Prod. No. O1008**), and long-chain amines (e.g., oleylamine).[2] Once nucleation has occurred, a homogeneous diffusion-controlled growth is observed across the solution during which the larger QDs grow more slowly than the smaller QDs, resulting in a size-focusing effect. As the growth progresses, Ostwald ripening occurs, in which the larger QDs continue to grow while the smaller QDs dissolve due to their higher chemical potential.[4] Until the point of saturation (see **Figure 1A**), the average particle size increases and the concentration of the particle decreases. The hot-injection method is particularly effective because it offers a high level of control over the size of the particles and size distribution by allowing a rapid nucleation separated from the growth stage. By varying the temperature, concentration of the surfactants, and reaction time, it is possible to obtain QDs of various sizes. Additionally, this method has also proven to be effective at synthesizing various types of QD nanocrystals.

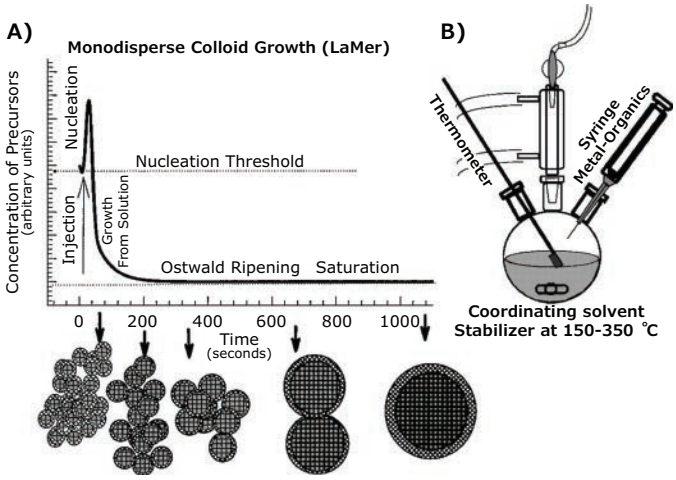

Figure 1. A) Schematic of the nucleation and growth stage for the preparation of monodisperse nanocrystals in the framework of the LaMer model. B) Representation of the simple synthetic apparatus employed to prepare monodisperse nanocrystals. Modified with permission from the Annual Review of Materials Science, Volume 30 Copyright Annual Reviews, http://www.annualreviews.org

Recently, the hot-injection method has been effectively adapted to synthesize all-inorganic cesium lead halide perovskite ($CsPbX_3$, X = Cl, Br, I) nanocrystals.[12] $CsPbX_3$ nanocrystals can be obtained by reacting Cs-oleate with a Pb(II)-halide in octadecene (**Prod. No. 74740**) at a high temperature (typically 140–200 °C) under N_2 atmosphere. Prior to injecting the Cs-oleate, a mixture of oleylamine and oleic acid at a 1:1 ratio is added to the Pb(II)-halide solution in octadecene (at 120 °C and N_2 atmosphere) to solubilize the Pb(II)-halide and stabilize the obtained nanocrystals. Due to the nature of the ionic metathesis reaction in $CsPbX_3$ nanocrystals, the nucleation and growth kinetics are very rapid, with the growth taking place within just 1–3 seconds. Therefore, the size of the $CsPbX_3$ nanocrystals can be tuned conveniently by varying the reaction temperature, but not varying the reaction time. The $CsPbX_3$ nanocrystals produced via this approach exhibit bandgap energies tunable by size and composition. This method can be employed to create $CsPbX_3$ nanocrystals that cover the entire visible spectral region with narrow emission line widths (12–42 nm) and exhibit a photoluminescence quantum yield (PLQY) ca. 50–90% (**Figure 2**).

The Heat-Up Method

The heat-up method is a non-injection approach that involves steadily heating the precursors in the presence of ligand. The heat-up method is generally considered to be a more efficient approach to preparing nanocrystals because it allows them to be prepared in a single pot without an injection step. The majority of the heat-up synthesis methods results in a polydisperse particle size-distribution because nucleation events are spread over an appreciable period of time. Cao et al. found that it is possible to obtain monodisperse CQDs with this method if

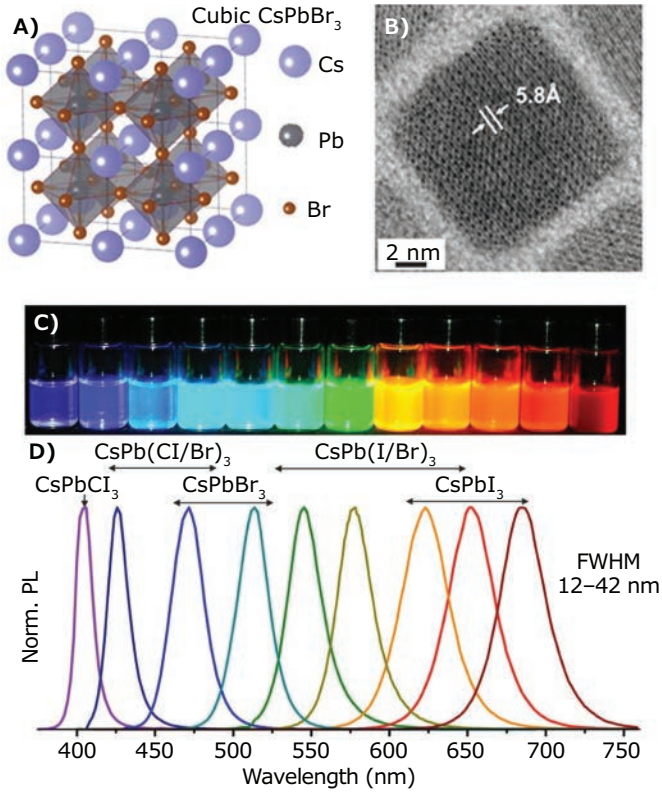

Figure 2. A) Schematic of the cubic perovskite lattice of $CsPbX_3$. B) Typical transmission electron microscopy (TEM) images of $CsPbBr_3$ NCs. C) Colloidal perovskite $CsPbX_3$ NCs in toluene under UV light. D) Representative PL spectra. Reproduced with permission from Reference 12. Copyright 2015 American Chemical Society.

precursors with a suitable level of reactivity are used. In a similar strategy to the hot-injection approach, the key is to employ a homogeneous nucleation process through the use of precursors that are highly reactive only when they reach a certain temperature. In general, the precursors should exhibit no, or very low, reactivity below the desired temperature to allow the predominance of growth in the target nanocrystals (**Figure 3**).[13]

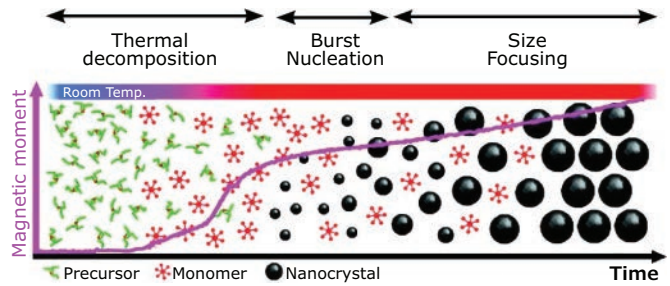

Figure 3. Schematic of the heat-up method.[14] Adapted with permission from Reference 14. Copyright 2007 American Chemical Society.

For example, it is possible to synthesize monodisperse CdSe QD nanocrystals in octadecene through the use of cadmium myristate, which decomposes at around 226 °C, and selenium powder (**Prod. No. 229865**), which decomposes at around 221 °C, as effective precursors at a growth temperature of 240 °C. In addition, selenium powder is only soluble in octadecene when the temperature exceeds 190 °C. As such, previous research has found that the nuclei appear when the temperature reaches around 210 °C, and this appearance is subsequently followed by constant growth. The concentration of the particles then increases to a maximum level before subsequently decreasing. This method proved to be an effective approach to synthesizing monodisperse (<5% standard deviation of sizes) and high-quality CQDs that have a PLQY of between 30–40%. In addition, a similar approach can be used to synthesize CdTe nanocrystals through the use of cadmium octadecylphosphonate and tributylphosphine telluride precursors.

The Cluster-Assisted Method

The cluster-assisted method utilizes very uniform clusters or seed particles within the reaction system. These act as nuclei and induce a controlled growth of the nanocrystals. The reaction is typically initiated by combining a known concentration of a small organometallic cluster with a coordinating solvent in the presence of semiconductor precursors (**Figure 4A**) before slowly increasing the temperature. This reaction seeding results in the clusters evolving into QD nucleation sites.

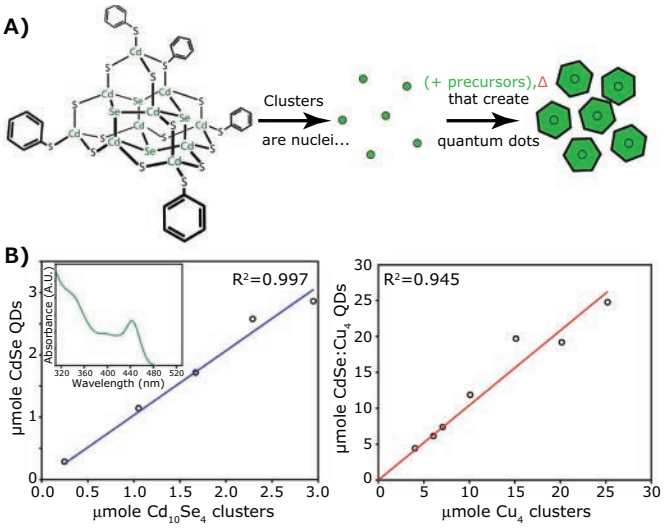

Figure 4. A) Schematic of cluster-seed method for synthesizing quantum dots. B) Graphic of concentration of the obtained quantum dots as a function of cluster concentration. Adapted with permission from Reference 15. Copyright 2013 American Chemical Society.

Snee et al. reported the use of the cluster-seeded approach to synthesize CdSe QDs using $(NMe_4)_4[Cd_{10}Se_4(SPh)_{16}]$ and $[Na(H_2O)_3]_2[Cu_4(SPh)_6]$ clusters.[15] They employed a typical synthesis process in which a certain quantity of the clusters was introduced into a mixture that consisted of octadecene (7 mL) and oleylamine (1 mL) with cadmium and selenium precursors (cadmium acetylacetonate, **Prod. No. 517585** and diphenylphosphine selenide **Prod. No. 802441** or tri-*n*-octylphosphine selenide). The mixture was subsequently stirred for 24 hours at a temperature of 50 °C under N_2 atmosphere. The study revealed that the presence of the cluster seeds directly impacted the concentration and size of the QDs. As **Figure 4B** shows, the resulting concentration of QDs was almost equal to the number of the cluster seeds (within 10%). Furthermore, the number of QDs produced via this method was approximately 20 times higher than that obtained via a standard rapid injection procedure that employs the same amount of precursors. In addition, increasing the cluster seed concentration decreased the size of the QDs due to the increasing number of QD nuclei competing for the finite number of available precursors. This approach has proven to be a versatile method of controlling the concentration of QDs and, furthermore, produces a large amount of QDs during a single reaction at a lower temperature.

The Microwave-Assisted Method

The microwave-assisted method of synthesizing nanocrystals offers excellent process control and allows elevated temperatures to be reached rapidly. This method is particularly convenient as the injection step is not required during the reaction, and the synthesis can take place under an air atmosphere. It is possible to avoid the variation in heating rate associated with conventional batch synthesis through the use of a microwave. When experimenting with the use of a microwave to synthesize nanocrystals, Strouse et al. were able to control the growth of CdTe and CdSe nanocrystals through selectively heating the chalcogenide precursor using microwave irradiation, which instantly activates the precursors that have a high polarizability. This activation is then followed by the nucleation and development of the nanocrystals.[16] In the microwave-assisted method, the growth rate can be controlled via a combination of reactant concentration and microwave power, while the particle size can be controlled by adjusting the reaction temperature. This approach to synthesis has been found particularly versatile and reproducible, offering a reaction time below 3 minutes, a very small standard deviation (6% for CdSe and 12% for CdTe) in terms of size across ten different reactions, and emission line widths of about 27–28 nm (CdSe) and 40 nm (CdTe).

In a standard microwave-assisted synthesis, cadmium stearate in alkane solvent is combined with the selenium powder in tri-*n*-octylphosphine inside a microwave reaction vessel at a 1:5 molar ratio of cadmium to selenium. Hexadecylamine (**Prod. No. 445312**) is added to the mixture before a septum is used to seal the vessel. Subsequently, the vessel is placed in a microwave and heated to a temperature of 240 °C with a ramping period of 30 seconds at a power of 300 W and a holding period of 30 seconds at 240 °C. The reaction is cooled immediately to room temperature. A study by Kappe et al. compared the conventional hot-injection method with the microwave-assisted method and found that the quality of the QDs obtained was identical for both sets of experiments.[17]

The Continuous-Flow Method

The continuous-flow approach offers some distinct advantages over batch synthesis; in particular, it offers a more viable path to mass production. When using a continuous flow reaction method, it is possible to readily automate and control the reaction parameters, achieve a more efficient process of optimization, enhance the efficiency with which the precursors are mixed, and increase the scalability. Recent developments in the design of the reactor used in the continuous-flow approach have delivered significant improvements in terms of the automation of a large-scale chemical reaction. Two-phase segmented-flow approaches (gas–liquid or liquid–liquid) solve the problems of slow diffusive mixing of precursors and broad residence time distribution that are inherent in the single-phase laminar flow design (**Figure 5A**). A two-phase segmented-flow also offers enhanced mixing of precursors and optimum heat and mass transfer in smaller volumes (isolated droplets) of chemical reactions, which have been shown to result in more monodispersed nanomaterials that are of a higher quality.[18,19]

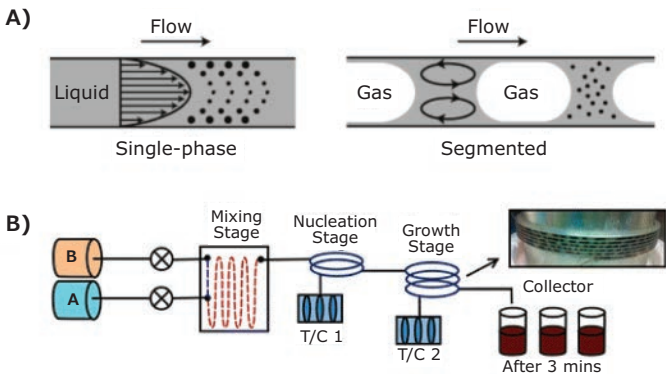

Figure 5. A) Schematic of mixing in single-phase and segmented gas–liquid flow synthesis. Reproduced with permission from Reference 18. Copyright 2005 Wiley Company. B) A dual-stage continuous-flow reactor setup that separates nucleation and growth stage. Reproduced with permission from Reference 20. Copyright 2013 American Chemical Society.

For example, PbS CQDs can be synthesized through the use of a dual-stage continuous-flow reactor system in combination with a two-phase segmented-flow approach (liquid–liquid). When the dual-stage system is employed, nucleation and growth take place in two separate reactors, allowing the application of different temperatures and subsequently providing more control over the nucleation process, as depicted in **Figure 5B**.[20] Two-phase segmentation is achieved by adding an inert, immiscible fluid (Fluorinert™ FC-70, **Prod. No. F9880**) into each precursor under stirring conditions. Precursor A contains lead oleate in octadecene, and precursor B contains bis(trimethylsilyl) sulfide (**Prod. No. 283134**) in octadecene. The two precursors are pumped into the mixer under N_2 overpressure. They then progress to the nucleation reactor at the temperature of nucleation (T_N) and, subsequently, the growth reactor at the temperature of growth (T_G). The reaction can also be controlled by manipulating the total residence time (t_R) of the reaction inside each reactor. By optimizing the parameters (T_N, T_G, t_R) in the dual-stage system, high-quality PbS CQDs can be synthesized with quality similar to that produced via the hot-injection method but with a greater production scalability. The typical production yield is 2.4–2.5 g/h.

Conclusions

Thanks to advances in synthetic methods, it is possible to synthesize monodisperse CQDs using a variety of approaches. Many of these approaches attempt to achieve similar outcomes in that they employ comparable mechanisms to obtain the homogeneous nucleation and controlled growth of monodisperse CQD nanocrystals. The hot-injection method is currently the most popular synthetic strategy to synthesize monodisperse CQDs. However, other methods, such as heat up, cluster assisted, microwave assisted, and continuous flow can offer sufficient advantages and versatility in terms of process efficiency. The heat-up method generally allows nanocrystals to be prepared in a single pot without an injection step. The microwave-assisted method of synthesizing nanocrystals is similar to the heat-up method but allows elevated temperatures to be reached rapidly, completing synthesis within minutes. The cluster-assisted method provides control over the concentration of QDs and enables a large amount of production but requires the judicious design of a suitable seed cluster. The continuous-flow assisted method represents an automated approach to producing high-quality CQD nanocrystals on a production scale. In the fabrication of QDs, a wide array of methods and synthetic tools are available. The selection criteria for each approach are dependent on the chemical composition and temperature requirements of the materials system, as well as the target production scale.

References

(1) Kim, J. Y.; Voznyy, O.; Zhitomirsky, D.; Sargent, E. H. *Adv. Mater.* **2013**, *25*(36), 4986–5010.
(2) Talapin, D. V.; Lee, J.-S.; Kovalenko, M. V.; Shevchenko, E. V. *Chem. Rev.* **2010**, *110*(1), 389–458.
(3) Pan, J.; Sarmah, S. P.; Murali, B.; Dursun, I.; Peng, W.; Parida, M. R.; Liu, J.; Sinatra, L.; Alyami, N.; Zhao, C.; Alarousu, E.; Ng, T. K.; Ooi, B. S.; Bakr, O. M.; Mohammed, O. F. *J. Phys. Chem. Lett.* **2015**, *6*(24), 5027–5033.
(4) Carey, G. H.; Abdelhady, A. L.; Ning, Z.; Thon, S. M.; Bakr, O. M.; Sargent, E. H. *Chem. Rev.* **2015**, *115*(23), 12732–12763.
(5) Ekimov, A. I.; Onushchenko, A. A. *JETP Lett.* **1981**, *34*(6), 345–349.
(6) Bodnarchuk, M. I.; Kovalenko, M. V. Engineering Colloidal Quantum Dots. In *Colloidal Quantum Dot Optoelectronics and Photovoltaics*; Konstantatos, G.; Sargent, E. H., Eds.; Cambridge University Press: Cambridge, **2013**; pp1–29.
(7) Kagan, C. R.; Lifshitz, E.; Sargent, E. H.; Talapin, D. V. *Science* **2016**, *353*(6302), 885.
(8) LaMer, V. K.; Dinegar, R. H. *J. Am. Chem. Soc.* **1950**, *72*(11), 4847–4854.
(9) Murray C. B.; Kagan, C. R.; Bawendi, M. G. *Annu. Rev. Mater. Sci.* **2000**, *30*(1), 545–610.
(10) Peng, X.; Wickham, J.; Alivisatos, A. P. *J. Am. Chem. Soc.* **1998**, *120*(21), 5343–5344.
(11) Murray, C. B.; Norris, D. J.; Bawendi, M. G. *J. Am. Chem. Soc.* **1993**, *115*(19), 8706–8715.
(12) Protesescu, L.; Yakunin, S.; Bodnarchuk, M. I.; Krieg, F.; Caputo, R.; Hendon, C. H.; Yang, R. X.; Walsh, A.; Kovalenko, M. V. *Nano Lett.* **2015**, *15*(6), 3692–3696.
(13) Yang, Y. A.; Wu, H.; Williams, K. R.; Cao, Y. C. *Angew. Chem., Int. Ed.* **2005**, *44*(41), 6712–6715.
(14) Kwon, S. G.; Piao, Y.; Park, J.; Angappane, S.; Jo, Y.; Hwang, N.-M.; Park, J.-G.; Hyeon, T. *J. Am. Chem. Soc.* **2007**, *129*(41), 12571–12584.
(15) Jawaid, A. M.; Chattopadhyay, S.; Wink, D. J.; Page, L. E.; Snee, P. T. *ACS Nano* **2013**, *7*(4), 3190–3197.
(16) Washington Ii, A. L.; Strouse, G. F. *J. Am. Chem. Soc.* **2008**, *130*(28), 8916–8922.
(17) Moghaddam, M. M.; Baghbanzadeh, M.; Keilbach, A.; Kappe, C. O. *Nanoscale* **2012**, *4*(23), 7435–7442.
(18) Yen, B. K. H.; Günther, A.; Schmidt, M. A.; Jensen, K. F.; Bawendi, M. G. *Angew. Chem.* **2005**, *117*(34), 5583–5587.
(19) Mehenni, H.; Sinatra, L.; Mahfouz, R.; Katsiev, K.; Bakr, O. M. *RSC Adv.* **2013**, *3*(44), 22397–22403.
(20) Pan, J.; El-Ballouli, A. a. O.; Rollny, L.; Voznyy, O.; Burlakov, V. M.; Goriely, A.; Sargent, E. H.; Bakr, O. M. *ACS Nano* **2013**, *7*(11), 10158–10166.

Materials for Quantum Dot Synthesis

For a complete list of available materials, visit **SigmaAldrich.com/metalsalts**.

Cadmium

Name	Composition	Purity	Form	Prod. No.
Cadmium bromide tetrahydrate	$CdBr_2 \cdot 4H_2O$	98%	solid	**336718-50G**
Cadmium carbonate	$CdCO_3$	98%	powder	**289140-100G** **289140-500G**
Cadmium chloride	$CdCl_2$	99.999% trace metals basis	beads	**439800-5G** **439800-25G**
	$CdCl_2$	99.99% trace metals basis	solid	**202908-10G** **202908-50G**
Cadmium chloride hydrate	$CdCl_2 \cdot xH_2O$	99.995% trace metals basis	solid	**529575-10G** **529575-50G**
		98%	solid	**208299-50G**
Cadmium iodide	CdI_2	99.999% trace metals basis	solid	**202916-10G**
		99%	solid	**228516-50G**
Cadmium nitrate tetrahydrate	$Cd(NO_3)_2 \cdot 4H_2O$	98%	solid	**642045-100G** **642045-500G**
Cadmium perchlorate hydrate	$Cd(ClO_4)_2 \cdot xH_2O$	-	crystals and lumps	**401374-25G**
Cadmium sulfate	$CdSO_4$	≥99.99% trace metals basis	solid	**481882-5G** **481882-25G**
Cadmium sulfate hydrate	$CdSO_4 \cdot xH_2O$	≥99.995% trace metals basis	powder and chunks	**202924-5G**

Cesium

Name	Composition	Purity	Form	Prod. No.
Cesium bromide	CsBr	99.999% trace metals basis	beads	**429392-1G** **429392-10G**
			powder and chunks	**203017-10G**
		99.9% trace metals basis	crystalline	**202142-100G**
Cesium carbonate	Cs_2CO_3	99.95% trace metals basis	powder	**554855-10G** **554855-50G**
Cesium chloride	CsCl	≥99.999% trace metals basis	crystalline	**203025-10G** **203025-50G**
		99.999% trace metals basis	beads	**449733-5G** **449733-25G**
		99.99% trace metals basis	powder	**562599-1KG** **562599-5KG**
Cesium fluoride	CsF	99.99% trace metals basis	solid	**255718-10G** **255718-50G**
Cesium hydroxide monohydrate	$HCsO \cdot H_2O$	99.95% trace metals basis	powder	**516988-5G** **516988-25G**
		≥99.5% trace metals basis	powder or crystals	**562505-1KG** **562505-5KG**
Cesium hydroxide hydrate	$HCsO \cdot xH_2O$	≥90% ≥99.5%, metals basis	powder, crystals or chunks	**C8518-10G** **C8518-50G** **C8518-250G**

Name	Composition	Purity	Form	Prod. No.
Cesium hydroxide solution	CsOH	99.9% trace metals basis	liquid	**232041-10G** **232041-50G** **232041-200G**
Cesium iodide	CsI	99.999% trace metals basis	beads	**429384-10G**
			solid	**203033-1G** **203033-10G**
		99.9% trace metals basis	powder	**202134-25G** **202134-100G**
Cesium nitrate	$CsNO_3$	99.99% trace metals basis	powder	**202150-10G** **202150-50G**
		99%	crystals and lumps	**289337-50G** **289337-250G**
Cesium sulfate	Cs_2O_4S	99.99% trace metals basis	powder and chunks	**230030-10G**

Indium

Name	Composition	Purity	Form	Prod. No.
Indium(I) bromide	InBr	99.998% trace metals basis	beads	**460605-5G** **460605-25G**
Indium(III) bromide	$InBr_3$	99.999% trace metals basis	solid	**545082-5G**
		99%	powder and chunks	**308285-10G** **308285-50G**
Indium(II) chloride	$InCl_2$	99.9% trace metals basis	powder	**548456-1G** **548456-10G**
Indium(III) chloride	$InCl_3$	≥99.999% trace metals basis	powder	**429414-5G** **429414-25G**
		99.999% trace metals basis	powder and chunks	**203440-1G** **203440-10G** **203440-50G**
		98%	powder	**334065-10G** **334065-50G**
Indium(III) chloride tetrahydrate	$InCl_3 \cdot 4H_2O$	97%	solid	**334073-5G** **334073-50G**
Indium(I) iodide	InI	99.999% trace metals basis	beads	**413658-1G** **413658-5G**
			powder	**578606-2G** **578606-10G**
Indium(III) iodide	InI_3	99.998% trace metals basis	powder	**413666-1G** **413666-5G**
Indium(III) nitrate hydrate	$In(NO_3)_3 \cdot xH_2O$	99.999% trace metals basis	crystals and lumps	**254215-10G** **254215-50G**
		99.99% trace metals basis	powder and chunks	**326127-10G** **326127-50G**
		99.9% trace metals basis	crystals and lumps	**326135-10G** **326135-50G**
Indium(III) sulfate hydrate	$In_2(SO_4)_3 \cdot xH_2O$	99.99% trace metals basis	solid	**288721-10G**

Lead

Name	Composition	Purity	Form	Prod. No.
Lead(II) bromide	$PbBr_2$	99.999% trace metals basis	powder	**398853-5G**
		≥98%	powder	**211141-100G** **211141-500G**
Lead(II) chloride	$PbCl_2$	99.999%	beads	**449865-5G**
Lead(II) chloride	$PbCl_2$	99.999% trace metals basis	powder and chunks	**203572-10G** **203572-50G**
		98%	powder	**268690-5G** **268690-250G** **268690-1KG**
Lead(II) fluoride	PbF_2	99.99% trace metals basis	powder and chunks	**229725-25G**
		≥99%	powder	**236152-100G** **236152-500G**
Lead(II) iodide	PbI_2	99.999% trace metals basis	beads	**554359-5G**
			solid	**203602-50G**
		99%	powder	**211168-50G**
Lead(II) iodide solution	PbI_2	-	solution	**795550-10ML**
Lead(II) sulfate	$PbSO_4$	99.995% trace metals basis	powder and chunks	**254258-10G** **254258-50G**
		98%	powder and chunks	**307734-100G** **307734-500G**
Methylammonium triiodoplumbate(II) precursor solution	$[CH_3NH_3]^+[PbI_3]^-$	-	solution	**793833-5ML**

Zinc

Name	Composition	Purity	Form	Prod. No.
Zinc bromide	$ZnBr_2$	99.999% trace metals basis	beads	**451398-5G** **451398-25G**
			powder and chunks	**230022-10G** **230022-50G**
Zinc chloride	$ZnCl_2$	99.999% trace metals basis	crystals and lumps	**229997-10G** **229997-50G** **229997-1KG**
		≥99.995% trace metals basis	powder	**429430-5G** **429430-25G**
		99.99% trace metals basis	amorphous beads	**450111-5G** **450111-10G** **450111-50G**
Zinc chloride solution	$ZnCl_2$	-	liquid	**703516-100ML** **703516-800ML**
Zinc citrate dihydrate	$(C_6H_5O_7)_2Zn_3 \cdot 2H_2O$	97%	powder	**480762-100G** **480762-500G**
Zinc cyanide	$Zn(CN)_2$	98%	-	**256498-5G** **256498-250G** **256498-1KG**
Zinc hexafluorosilicate hydrate	$ZnSiF_6 \cdot xH_2O$	99%	solid	**401498-100G**
Zinc iodide	ZnI_2	99.999% trace metals basis	beads	**409278-5G**
			powder	**466360-5G** **466360-25G**
		≥99.99% trace metals basis	crystalline	**230014-25G**
		≥98%	powder	**223883-50G** **223883-250G**
Zinc nitrate hydrate	$Zn(NO_3)_2 \cdot xH_2O$	99.999% trace metals basis	powder and chunks	**230006-25G** **230006-250G**
Zinc perchlorate hexahydrate	$Zn(ClO_4)_2 \cdot 6H_2O$	-	crystals and lumps	**401439-100G** **401439-500G**
Zinc phosphate	$Zn_3(PO_4)_2$	99.998% trace metals basis	powder and chunks	**587583-5G** **587583-25G**
Zinc sulfate heptahydrate	$ZnSO_4 \cdot 7H_2O$	99.999% trace metals basis	powder, crystals or chunks	**204986-10G** **204986-50G**

Other

Name	Composition	Purity	Form	Prod. No.
Diphenylphosphine selenide	$C_{12}H_{11}PSe$	95%	powder or crystals	**802441-1G**
Selenium oxychloride	$SeOCl_2$	97%	liquid	**336157-10G**
Selenium tetrachloride	$SeCl_4$	-	powder or crystals	**323527-10G** **323527-50G**
Sulfur monochloride	S_2Cl_2	98%	liquid	**157759-50G** **157759-250G** **157759-1KG**
Tellurium tetrachloride	$TeCl_4$	99%	powder, crystals or chunks	**205338-5G** **205338-25G** **205338-100G**

Nanowire Synthesis: From Top-Down to Bottom-Up

David J. Hill, James F. Cahoon*

Department of Chemistry, University of North Carolina at Chapel Hill, USA
*Email: jfcahoon@unc.edu

Introduction

The properties of many devices are limited by the intrinsic properties of the materials that compose them. However, at the nanoscale, device properties are no longer dependent solely on the material type, but also on material geometry (for example, transforming glass into the brilliant colors of an opal). Nanowires, anisotropic structures with diameters from one to hundreds of nanometers and lengths of tens to hundreds of microns, provide a unique platform for harnessing these nanoscale phenomena.

Many nanowires are single crystals, and as a result of their narrow diameter have an extremely high surface area. This high surface-area-to-volume ratio makes nanowires very sensitive to changes in surface chemistry and gives rise to their prevalence in sensor development.[1] Nanowire diameters are also sufficiently small to allow the penetration of biological structures without damage, while their length allows them to transport signals in and out of a cell.[1] These properties also make nanowires very effective as battery electrodes, with long conduction pathways that achieve high conductivity and high surface area that permits rapid charging.[2]

Some of the largest potential gains from nanowires come from exploiting the properties that only appear on the nanoscale. The diameter of a nanowire is less than the wavelength of visible light; as a result, a nanowire operates in the wave-optics regime. Absorption and reflectivity can be tuned by manipulating nanowire geometry to select specific optical modes.[3] Similarly, nanowires are below the mean free path for phonons, permitting a reduction of thermal conductivity below the bulk limit.[1] The mechanical properties of nanowires also differ from those of the bulk material due to the ability of a nanowire to dissipate strain at its surface.[1] In order to produce and utilize these properties, reliable and controllable nanowire syntheses are required, but synthetic methods vary widely in how the extremely anisotropic structures are generated. Broadly speaking, synthesis techniques can be divided into two categories: top-down fabrication and bottom-up synthesis.

Top-Down Fabrication

Conventional top-down nanowire fabrication is a subtractive technique, like carving a statue from a block of marble, using chemicals rather than chisels to achieve nanoscale control. It utilizes many of the techniques employed by the semiconductor industry, such as lithography and chemical etching, to turn a bulk wafer or crystal into nanowire structures. In general, top-down fabrication relies on large, expensive, and precise instrumentation that can be found in cleanroom and nanofabrication facilities.

Lithography

Among the most popular top-down techniques for nanofabrication is lithography, which is used extensively in the microelectronics industry. This technique involves the deposition of a resist material, such as poly(methylmethacrylate) that will act like photographic film to produce a pattern after exposure and development using a patterned mask. The resolution of photolithography is limited by the lithographic technique and wavelength of light used, and it is often not suitable or practical for small nanowires. Patterns with higher resolution can be achieved with electron-beam lithography, which is a maskless direct-write exposure method. For the production of vertical nanowires, the pattern will consist of a series of circles or holes on top of a wafer of the target material. For horizontal nanowires, the pattern will be a series of lines or trenches on a layered substrate, such as silicon-on-insulator (SOI).

Nanowires can then be produced by etching the extraneous material from the wafer. Depending on the process, the resist may be used directly as the etch mask or may serve as the template for deposition of a more stable mask material, such as gold. Wet chemical etchants, like potassium hydroxide (**Prod. No. 306568**), or an electrochemical etchant can then be used to etch the pattern, as illustrated in **Figure 1A**. This technique often produces tapered rather than cylindrical wires due to etching underneath the mask. This problem can be minimized by the use of anisotropic etchants, but it is rarely completely eliminated.[4] One approach to achieving cylindrical vertical wires is to replace the wet chemical etch with a highly anisotropic

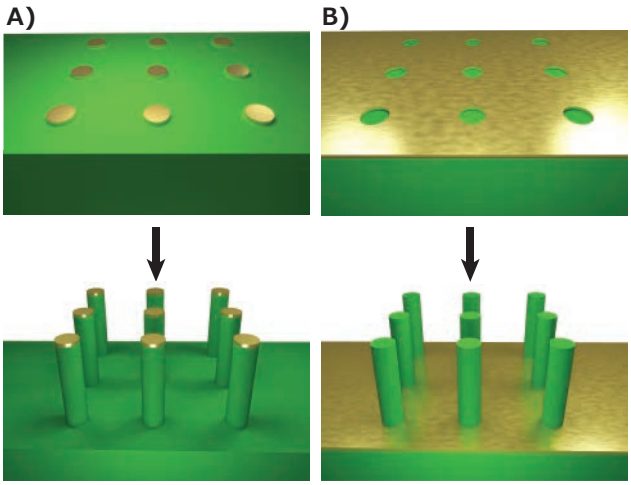

Figure 1. Top-down fabrication methods. **A**) Lithographic patterning of a metallic mask followed by anisotropic etching, such as DRIE. **B**) Lithographic patterning of exposed regions followed by anisotropic metal-assisted chemical etching.

deep reactive ion etch (DRIE), which can achieve vertical nanowires that are tens of microns in length. Alternatively, the pattern can be inverted and metal-assisted etching used,[5] illustrated in **Figure 1B**, to achieve similar anisotropic structures.

Alternate approaches to conventional lithography promise higher resolution than can be achieved with optical lithography and higher throughput than is possible with conventional methods. Nanosphere lithography (NSL), for instance, involves the self-assembly of a monolayer of polystyrene nanospheres onto a substrate in a close-packed lattice.[6] These spheres serve as a mask for the deposition of a metal or other masking material and are subsequently removed after deposition. Nanoscale patterns also can be produced through mechanical transfer with nano-imprint lithography (NIL).[7] A high resolution master pattern is produced with a cost-intensive technique such as electron-beam lithography. This master is then pressed into the resist material to transfer the pattern.

Benefits and Issues

Top-down nanowire fabrication is enticing due to the ease with which ordered arrays of nanowires can be constructed. This facilitates electrical contact to the nanowires and their integration into large-scale devices. Additionally, many of these processes are compatible with standard microelectronics industry processes, enabling their scale up.

Top-down fabrication does present several drawbacks. The applicability of photolithography to these processes diminishes as the desired length scales decrease, requiring the implementation of more advanced methods such as extreme ultraviolet (EUV) lithography. Alternatives to photolithography, like electron-beam and scanning probe lithographies, are direct-write techniques, requiring slow serial writing of individual elements. Parallelization of these techniques will be necessary for industrial-scale production. Nanowires formed by top-down processes also frequently lack complex electronic characteristics. When etched from a wafer, any desired modulation of composition must be encoded into the wafer by techniques like molecular beam epitaxy (MBE) or encoded after growth through implantation methods. This processing can greatly increase the material cost of nanowire devices compared to bottom up techniques.

Bottom-Up Synthesis

In contrast to top-down techniques, bottom-up processes are derived from a chemist's toolkit, where molecules are assembled piece-by-piece and scaled up to produce materials thousands of times larger than the average molecule. Bottom-up syntheses are additive, like the growth of a tree from a small seed, using chemistry to control structure.

Vapor Phase

The anisotropic growth of nanowires is frequently accomplished using nanoparticle catalysts and gas-phase precursors. One of the most common methods is vapor-liquid-solid (VLS) growth, wherein gaseous precursors of the desired nanowire material, such as $SiCl_4$ (**Prod. No. 215120**) for silicon, dissolve into a liquid-metal catalyst.[8] As the catalyst becomes supersaturated, the solid nanowire crystallizes from the liquid catalyst, as illustrated in **Figure 2A**. This synthesis involves a chemical vapor deposition (CVD) system, in which the temperature, pressure, and flow rates of precursors can be regulated. The conditions must be controlled to minimize non-catalytic growth of material on the side of the nanowire, which would disrupt the cylindrical geometry. Noble metal nanoparticles commonly serve as the initial seed for nanowire growth. For the VLS process, the metal must form a liquid droplet that serves as the catalyst. In many cases, this droplet forms a eutectic composition that melts at a lower temperature than the pure metal or semiconductor material. However, when synthesizing binary or ternary materials that contain a low melting metal, such as Ga in GaAs, the VLS process can be self-catalyzed using a Ga liquid droplet that is continuously supplied by a vapor-phase precursor such as trimethylgallium (**Prod. No. 730734**).

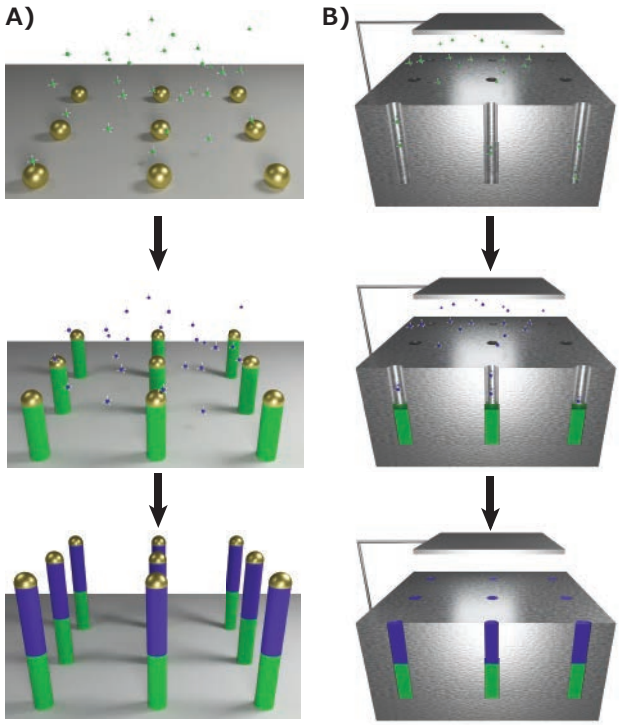

Figure 2. Bottom-up synthesis methods. **A**) Vapor-phase growth of segmented nanowires through the VLS process, with modulation of the gaseous precursor resulting in controlled compositional changes. **B**) Solution-phase growth of nanowires through electrochemical deposition into anodic aluminum oxide (AAO). A similar segmentation process is possible.

VLS processes are advantageous because they allow for compositional control. Dopant materials, such as phosphine for silicon, can be introduced and removed repeatedly throughout the nanowire growth, producing superlattice structures with modulated electronic properties.[9] Similarly, changing the ratio of the components in a ternary structure, like $GaAs_xP_{1-x}$, can produce nanometer-scale bandgap modulation[10] and quantum-well structures.

Although metal catalysts are commonly dispersed on a solid substrate, a variant called aerotaxy utilizes catalysts suspended in the reactor to achieve high growth rates.[11] A lower temperature process, called vapor-solid-solid (VSS) growth, uses many of the same principles as VLS growth.[12] However, the catalysts are solid rather than liquid, altering the kinetic processes. Rather than dissolving and supersaturating in a liquid, the precursors diffuse through the interface between the catalyst and nanowire in order to add material. This slows down the growth process, allowing for more abrupt (to the atomic level) compositional changes in the nanowire.

Contamination of the catalyst material in the nanowire can be disadvantageous for certain processes, so non-catalyzed syntheses have also been developed. Templated growth provides one pathway to achieve the anisotropy needed for nanowires. AAO, produced by electrochemical etching, contains a honeycomb of nanometer-scale channels, offering the geometry required for producing arrays of vertical nanowires. Conventional vapor deposition techniques (CVD, sputtering, etc.) can be used to fill these channels, producing nanowires when the template is removed. A patterned substrate can be used for selective-area epitaxy (SAE), in which epitaxial growth occurs in exposed regions, but deposition onto the mask material does not occur.[13] The presence of screw dislocations has also been demonstrated as a mechanism to induce catalyst-free nanowire growth.[14]

Solution Phase

Many of the techniques employed in the vapor phase have analogies in the liquid phase. The solution-liquid-solid (SLS) mechanism is similar to that of VLS, except nanowire precursors are dissolved into a high-boiling liquid, such as squalane (**Prod. No. 234311**), and the catalysts are suspended therein.[15] AAO substrates can also be used for templated solution growth, using electrochemical deposition to fill the channels[16] as shown in **Figure 2B**. Drawing upon the solution-phase synthesis of nanoparticles, redox reactions can also be used to produce nanowires.[17] Seed particles are first grown by a rapid reduction of a dissolved precursor with a strong reducing agent like sodium borohydride. Secondary growth is achieved with a weaker reducing agent, like L-ascorbic acid, to prevent additional seed particle production. The nanowire anisotropy is achieved by controlling surface chemistry. The introduction of surfactants that selectively alter the surface energy of particular crystal facets, such as hexadecyltrimethylammonium bromide (CTAB, **Prod. No. 52370**), directs growth along particular axes, producing nanowires.

Benefits and Issues

Bottom-up synthesis provides the opportunity for explicit control of nanowire composition during growth, enabling the production of complex superlattice structures. This compositional control can be used to encode novel electronic properties such as quantum well photodiodes, as well as provide a template for subsequent processing. Selective etching of these superlattice structures has been shown to produce a wide variety of shapes and structures that can be used in photonics, electronics, and memory[18] (**Figure 3**).

The main challenge facing further development of technologies based on bottom-up nanowires involves their integration into large-scale devices. Wires grown in vertical arrays can be used in a similar fashion to those fabricated by top-down methods, but many growth processes instead produce disordered "forests" of nanowires or solutions of nanowires. Recent research efforts have focused on how to assemble and organize the nanowires so they can be interfaced with conventional manufacturing steps. The incorporation of these techniques will prove essential to moving nanowires from the laboratory to the factory.

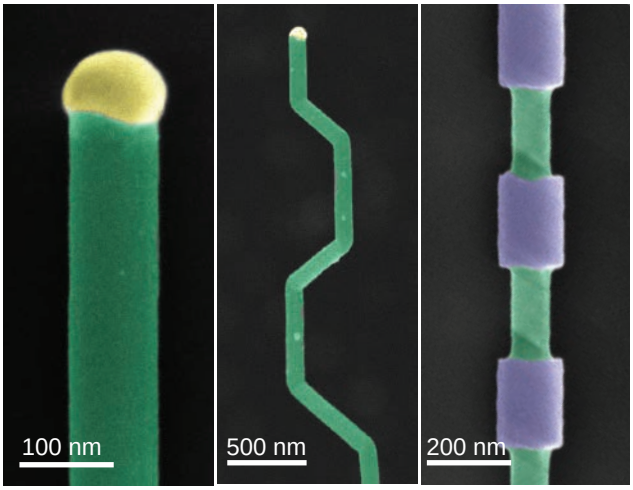

Figure 3. Nanowire structures. A) False-color SEM of a silicon nanowire grown by VLS (green) and the metal catalyst at the tip (yellow). B) False-color SEM of crystallographic kinking that can be accomplished by manipulating the reaction conditions. C) False-color SEM of morphology that can be achieved by modulating the composition during growth, followed by etching.

Conclusions

Nanowires possess a number of unique properties derived from their highly anisotropic but often single-crystalline structure. They are highly sensitive to changes in surface chemistry due to their high surface area. They also provide for highly anisotropic charge transport, allowing for rapid radial transport or charge injection combined with long conduction pathways along the nanowire axis. The diameter of nanowires is sufficiently small to allow many bulk properties to be manipulated by the nanowire geometry. Nanowire optical properties can be tuned by manipulating the diameter, which changes the optical resonant modes that can be supported by the nanowire. Similarly, thermal transport can be altered through nanoscale geometry. Due to their small radii, nanowires can relieve strain more efficiently than bulk materials, making them much more flexible.

The primary concern that underlies nanowire synthesis or fabrication is how to achieve the necessary anisotropy. Top-down fabrication techniques utilize bulk crystals and use patterning to selectively remove material to produce nanowires. Conversely, bottom-up techniques grow the nanowires from reactive precursors, using nanoparticles or nanostructured templates to provide the anisotropy. The complementary integration of top-down and bottom-up techniques will be vital to the integration of nanowires with industrial processes. Nanowires present an opportunity to overcome bulk material limitations through nanoscale electronic and structural control, which will enable a new generation of devices and applications.

References

(1) Dasgupta, N. P.; Sun, J.; Liu, C.; Brittman, S.; Andrews, S. C.; Lim, J.; Gao, H.; Yan, R.; Yang, P. *Adv. Mater.* **2014**, *26*, 2137–2184, doi:10.1002/adma.201305929.
(2) Shao, M.; Ma, D. D. D.; Lee, S.-T. *Eur. J. Inorg. Chem.* **2010**, 4264–4278, doi:10.1002/ejic.201000634.
(3) Tian, B.; Kempa, T. J.; Lieber, C. M. *Chem. Soc. Rev.* **2009**, *38*, 16–24, doi:10.1039/b718703n.
(4) Wu, B.; Kumar, A.; Pamarthy, S. *J. Appl. Phys.* **2010**, *108*, 051101, doi:10.1063/1.3474652.
(5) Huang, Z.; Geyer, N.; Werner, P.; de Boor, J.; Gosele, U. *Adv. Mater.* **2011**, *23*, 285–308, doi:10.1002/adma.201001784.
(6) Cheung, C. L.; Nikolić, R. J.; Reinhardt, C. E.; Wang, T. F. *Nanotechnology* **2006**, *17*, 1339–1343, doi:10.1088/0957-4484/17/5/028.
(7) Chou, S. Y.; Krauss, P. R.; Renstrom, P. J. *Science* **1996**, *272*, 85–87, doi:10.1126/science.272.5258.85.
(8) Wagner, R. S.; Ellis, W. C. *Appl. Phys. Lett.* **1964**, *4*, 89–90, doi:10.1063/1.1753975.
(9) Christesen, J. D.; Pinion, C. W.; Hill, D. J.; Kim, S.; Cahoon, J. F. *J. Phys. Chem. Lett.* **2016**, *7*, 685–692, doi:10.1021/acs.jpclett.5b02444.
(10) Gudiksen, M. S.; Lauhon, L. J.; Wang, J.; Smith, D. C.; Lieber, C. M. *Nature* **2002**, *415*, 617–620, doi:10.1038/415617a.
(11) Heurlin, M.; Magnusson, M. H.; Lindgren, D.; Ek, M.; Wallenberg, L. R.; Deppert, K.; Samuelson, L. *Nature* **2012**, *492*, 90–94, doi:10.1038/nature11652.
(12) Hobbs, R. G.; Petkov, N.; Holmes, J. D. *Chem. Mater.* **2012**, *24*, 1975–1991, doi:10.1021/cm300570n.
(13) Hamano, T.; Hirayama, H.; Aoyagi, Y. *Jpn. J. Appl. Phys.* **1997**, *36*, L286–L288, doi:10.1143/jjap.36.l286.
(14) Bierman, M. J.; Lau, Y. K.; Kvit, A. V.; Schmitt, A. L.; Jin, S. *Science* **2008**, *320*, 1060–1063, doi:10.1126/science.1157131.
(15) Heitsch, A. T.; Fanfair, D. D.; Tuan, H. Y.; Korgel, B. A. *J. Am. Chem. Soc.* **2008**, *130*, 5436–5437, doi:10.1021/ja8011353.
(16) Qin, L.; Park, S.; Huang, L.; Mirkin, C. A. *Science* **2005**, *309*, 113–115, doi:10.1126/science.1112666.
(17) Sun, Y.; Gates, B.; Mayers, B.; Xia, Y. *Nano Lett.* **2002**, *2*, 165–168, doi:10.1021/nl010093y.
(18) Christesen, J. D.; Pinion, C. W.; Grumstrup, E. M.; Papanikolas, J. M.; Cahoon, J. F. *Nano Lett.* **2013**, *13*, 6281–6286, doi:10.1021/nl403909r.

Precursors Packaged for Deposition Systems

For a complete list of available materials, visit **SigmaAldrich.com/ald**.

Name	Acronym	Structure	Form	Prod. No.
(3-Aminopropyl)triethoxysilane	APTES; APTS	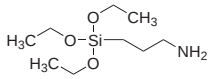	liquid	**706493-20ML**
Bis(methyl-η⁵–cyclopentadienyl) methoxymethylzirconium	ZrD-CO_4; ZRCMMM	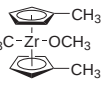	liquid	**725471-10G**
Diethylzinc	DEZ; DEZn; Et_2Zn	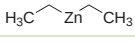	liquid	**668729-25G**
Niobium(V) ethoxide	NbOEt	$Nb(OCH_2CH_3)_5$	liquid	**760412-10G**
Silicon tetrachloride	STC	$SiCl_4$	liquid	**688509-25ML**
Tetrakis(diethylamido)titanium(IV)	TDEAT	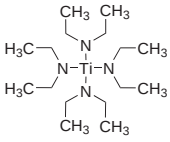	liquid	**725536-10G**

Name	Acronym	Structure	Form	Prod. No.
Tetrakis(dimethylamido)hafnium(IV)	TDMAH	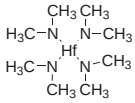	low-melting solid	**666610-25G**
Tetrakis(dimethylamido)titanium(IV)	TDMAT	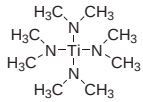	liquid	**669008-25G**
Tetrakis(dimethylamido)zirconium(IV)	TDMAZ	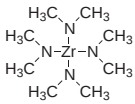	solid	**669016-25G**
Tetrakis(ethylmethylamido)hafnium(IV)	TEMAH	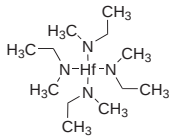	liquid	**725544-10G**
Tetrakis(ethylmethylamido) zirconium(IV)	TEMAZ	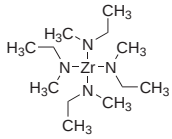	liquid	**725528-10G**
Titanium(IV) isopropoxide	TTIP	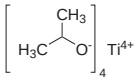	liquid	**687502-25G**
Titanium tetrachloride	TTC	$TiCl_4$	liquid	**697079-25G**
Triethylgallium	TEG; TEGa; Et_3Ga	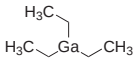	liquid	**730726-10G**
Trimethylaluminum	TMA		liquid	**663301-25G**
Trimethylgallium	TMG; TMGa; Me_3Ga	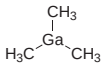	liquid	**730734-10G**
Trimethyl(methylcyclopentadienyl) platinum(IV)	$MeCpPtMe_3$	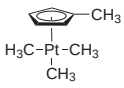	low-melting solid	**697540-10G**
Tris[N,N-bis(trimethylsilyl)amide] yttrium	YTDTMSA	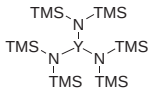	powder	**702021-10G**
Tris(diethylamido)(tert-butylimido) niobium(V)	-	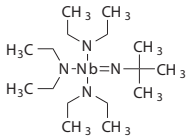	liquid	**751774-10G**
Tris(diethylamido)(tert-butylimido) tantalum(V)	TBTDET	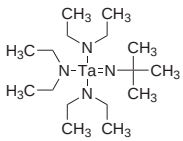	liquid	**668990-10G**
Tris(dimethylamino)silane	TDMAS	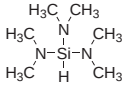	liquid	**759562-25G**
Tungsten hexacarbonyl	-	$W(CO)_6$	solid	**755737-25G**
Water	-	H_2O	liquid	**697125-25ML**
Zirconium(IV) tert-butoxide	ZTB	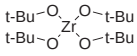	liquid	**759554-25G**

Solution Deposition Precursors for Nanomaterial Growth

For a complete list of available materials, visit **SigmaAldrich.com/solutiondeposition**.

Name	Structure	Purity	Form	Prod. No.
Aluminum acetylacetonate	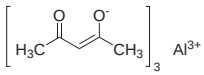	99%	solid	**208248-100G** **208248-500G**
Aluminum isopropoxide	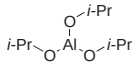	≥98%	solid	**220418-100G** **220418-1KG**
Indium(III) acetate	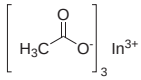	99.99% trace metals basis	solid	**510270-10G** **510270-50G**
Indium(III) acetylacetonate	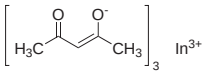	≥99.99% trace metals basis	solid	**I3300-5G**
Iron(II) acetate	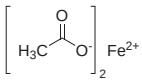	≥99.99% trace metals basis	solid	**517933-5G** **517933-25G**
Iron(III) acetylacetonate	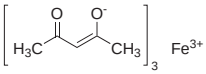	≥99.9% trace metals basis	powder	**517003-10G** **517003-50G**
Lead(II) acetate trihydrate	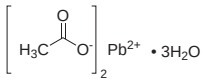	99.999% trace metals basis	solid	**316512-5G** **316512-25G** **316512-100G**
Lithium acetate		99.95% trace metals basis	powder or crystals	**517992-100G**
Niobium(V) ethoxide	$Nb(OCH_2CH_3)_5$	99.95% trace metals basis	liquid	**339202-5G** **339202-50G**
Palladium(II) acetylacetonate	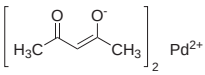	99%	-	**209015-1G** **209015-5G**
Potassium tert-butoxide solution		-	liquid	**328650-50ML** **328650-500ML** **328650-2L** **328650-20L**
Silver trifluoroacetate		98%	powder	**T62405-5G** **T62405-25G**
Tantalum(V) ethoxide	$(CH_3CH_2O)_5Ta$	99.98% trace metals basis	liquid	**339113-10G** **339113-100G**
Tetraethyl orthosilicate	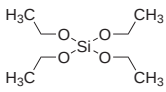	99.999% trace metals basis	liquid	**333859-25ML** **333859-100ML**
		98%	liquid	**131903-25ML** **131903-250ML** **131903-500ML** **131903-1L** **131903-2.5L** **131903-4L**
Tetramethyl orthosilicate	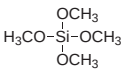	98%	liquid	**218472-100G** **218472-500G**
Thallium(I) acetate		≥99%	powder	**T8266-5G** **T8266-25G** **T8266-100G**
Tin(II) acetylacetonate	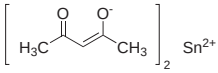	99.9% trace metals basis	-	**697478-5G**
Titanium diisopropoxide bis(acetylacetonate)	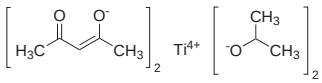	-	solution	**325252-100ML** **325252-500ML**
Titanium(IV) ethoxide	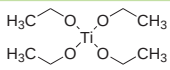	-	liquid	**244759-50G** **244759-250G**
Titanium(IV) isopropoxide	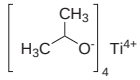	99.999% trace metals basis	liquid	**377996-5ML** **377996-25ML** **377996-100ML**

Name	Structure	Purity	Form	Prod. No.
Zinc acetate dihydrate	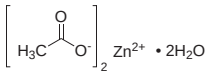	99.999% trace metals basis	powder or chunks	**379786-5G** **379786-25G**
Zirconium acetate solution	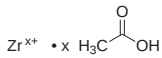	-	liquid	**413801-500ML** **413801-2L**
Zirconium(IV) propoxide solution	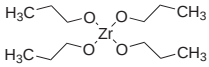	-	solution	**333972-5ML** **333972-100ML** **333972-500ML**

Vapor Deposition Precursors for Nanomaterial Growth

For a complete list of available materials, visit **SigmaAldrich.com/vapordeposition.**

Name	Structure	Purity	Form	Prod. No.
(3-Aminopropyl)triethoxysilane	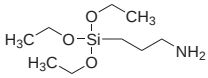	≥98.0%	liquid	**741442-100ML** **741442-500ML**
Bis(cyclopentadienyl)cobalt(II)		-	solid powder or crystals	**339164-2G** **339164-10G**
Hexamethyldisilazane	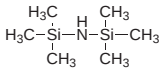	99.9%	liquid	**379212-25ML** **379212-100ML**
		≥99%	liquid	**440191-100ML** **440191-1L**
Iron(0) pentacarbonyl	$Fe(CO)_5$	>99.99% trace metals basis	liquid	**481718-25ML** **481718-100ML**
Manganese(0) carbonyl	$Mn_2(CO)_{10}$	98%	powder or crystals	**245267-1G** **245267-10G**
Molybdenumhexacarbonyl	$Mo(CO)_6$	≥99.9% trace metals basis	solid solid	**577766-5G** **577766-25G**
		98%	solid	**199958-10G** **199958-50G** **199958-250G**
Silicon tetrachloride	$SiCl_4$	99%	liquid	**215120-100G** **215120-1KG**
Tetrakis(dimethylamido)titanium(IV)	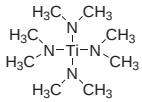	99.999% trace metals basis	liquid	**469858-5G** **469858-25G**
Tetrakis(dimethylamido)zirconium(IV)	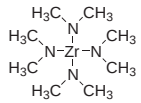	≥99.99% trace metals basis	solid	**579211-5G**
Tetrakis(ethylmethylamido) hafnium(IV)	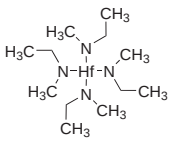	≥99.99% trace metals basis	liquid	**553123-5ML** **553123-25ML**
Trimethylaluminum		97%	liquid	**257222-100G**
Trimethyl(methylcyclopentadienyl) platinum(IV)	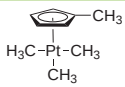	98%	low-melting solid	**645605-2G**
Triphenylborane	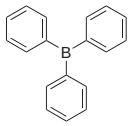	-	solid powder	**T82201-2.5G** **T82201-10G**

Name	Structure	Purity	Form	Prod. No.
Tris(pentafluorophenyl)borane	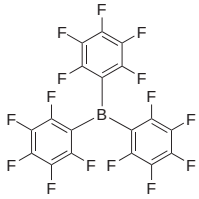	95%	powder	**442593-1G-A** **442593-5G-A**
Tungsten hexacarbonyl	$W(CO)_6$	99.99% trace metals basis (excluding Mo)	solid	**472956-5G** **472956-25G**
		97%	solid	**241431-10G** **241431-50G**

Sputtering Targets

For a complete list of available materials, visit **SigmaAldrich.com/sputtering-target**.

Name	Diam. × Thickness (in.)	Purity (% trace metals basis)	Prod. No.
Aluminum	3.00 × 0.125	99.9995	**749036-1EA**
Aluminum zinc oxide	3.00 × 0.125	99.99	**752665-1EA**
Chromium	3.00 × 0.125	99.95	**749052-1EA**
Copper	2.00 × 0.25	99.95	**767476-1EA**
Indium tin oxide	3.00 × 0.125	99.99	**752657-1EA**
Nickel	2.00 × 0.25	99.95	**767484-1EA**
Silicon	2.00 × 0.25	99.999	**767492-1EA**
Tantalum	2.00 × 0.25	99.95	**767514-1EA**
Titanium	3.00 × 0.125	99.995	**749044-1EA**
	2.00 × 0.25	99.995	**767506-1EA**
Tungsten	2.00 × 0.25	99.95	**767522-1EA**
Yttrium(III) oxide	2.00 × 0.25	99.99	**774022-1EA**
Yttrium sputtering target	2.00 × 0.25	99.9	**773972-1EA**
Zinc	3.00 × 0.125	99.995	**749060-1EA**
Zinc oxide	3.00 × 0.125	99.99	**752681-1EA**
Zirconium(IV) oxide	2.00 × 0.25	99.95 (excludes 2% HfO_2)	**774030-1EA**
Zirconium(IV) oxide-yttria stabilized	2.00 × 0.25	99.9	**774049-1EA**
Zirconium yttrium alloy	2.00 × 0.25	99.9 (excluding <=1% Hf)	**774057-1EA**

Building and Engineering Micro/Nano Architectures of Single-Walled Carbon Nanotubes for Electronic Applications

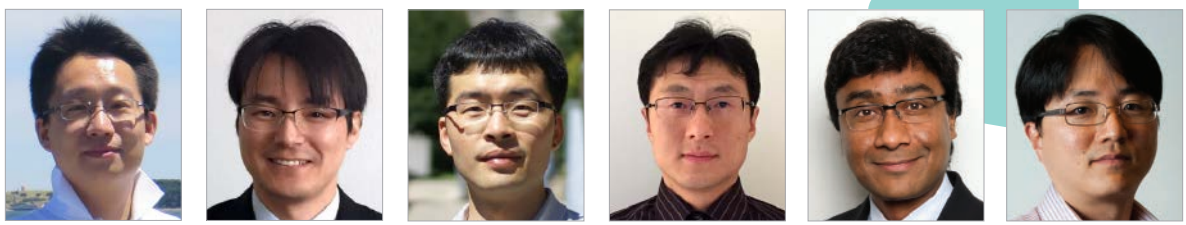

Ji Hao,[1] Hyunyoung Jung,[1] Younglae Kim,[1] Bo Li,[1,3] Swastik Kar,[2] Yung Joon Jung[1*]

[1]Department of Mechanical and Industrial Engineering, Northeastern University, Boston, MA 02115, USA
[2]Department of Physics, Northeastern University, Boston, MA 02115, USA
[3]Department of Mechanical Engineering, Villanova University, Villanova, PA 19085, USA
*Email: y.jung@northeastern.edu

Introduction

Single-walled carbon nanotubes (SWCNTs) continue to attract significant research interest over two decades since the discovery of carbon nanotubes (CNTs) by Iijima.[1] Their molecular structure can best be described as graphene rolled up into a one-dimensional (1-D) seamless cylinder. The unique quasi 1-D structure and aromatic monolayer[2,3] surface provides exceptional electrical properties (high current-carrying capacities, ~10^9 Acm^{-2}),[4,5] thermal conductivity (~3,500 $Wm^{-1}K^{-1}$),[6] and mechanical properties (Young's moduli, ~1–2 TPa).[7] These properties make SWCNTs an ideal candidate for various applications including sensors,[8] energy storage devices,[9] field emitting devices,[10] and drug delivery agents.[11] In order to make an integrated electronic device using SWCNTs as a main component, it is important to develop manufacturing processes that: i) controllably assemble SWCNTs in desired locations, orientations, and dimensions; ii) integrate them into highly functional devices; and iii) engineer their molecular structures in order to further enhance their physical properties.

In this article, we present our state-of-the-art self-assembly method for fabricating highly organized and controlled micro- and nanoscale SWCNT networks on various substrates.[12–14] Second, we demonstrate integration of these organized architectures for application in an optoelectronic device by creating highly controlled heterojunctions of SWCNTs and silicon. This represents a new kind of photodiode-based logic device that can be controlled by both optical and electrical input with high voltage-switchable photocurrent responsivity (>1 A/W), photovoltage responsivity (>10^5 V/W), and good electrical and optical on/off ratio (electrical: >10^5 and optical: >10^4).[15] Third, we demonstrate the use of these SWCNT networks for high performance hydrogen sulfide (H_2S) detection by functionalizing with 2,2,6,6-tetramethylpiperidine-1-oxyl (TEMPO, **Prod. No. 426369**).[16] Finally, we introduce the structural transformation of SWCNT networks to continuous multiwalled carbon nanotubes and then onto the graphite/multilayered graphene nanoribbon structures by using a newly developed voltage-controlled electrical treatment method called, "nanotube fusion," which not only demonstrates the new method to engineer the sp^2 structures of carbon nanotubes, but also greatly improves their electrical and thermal transport properties.[17]

Assembly of SWCNT Networks

The method we used to fabricate highly organized and aligned SWCNT thin films is a template-guided fluidic assembly, which employs a lithographically patterned template-assisted dip coating.[12–14,18] SWCNTs were directly assembled on a hydrophilic surface, between predesigned photoresist channels, forming highly originated SWCNT lateral networks in micro- and nanoscale. The quality of fluidic assembly can be improved when the substrates are treated with plasmas, which increases the number of dangling bonds and hydrophilic hydroxide functional groups on the surface. **Figure 1** shows the detailed procedures of the template-guided fluidic assembly method. **Figures 1A–C** show the SiO_2 substrate was treated by plasmas, then spin-coated by photoresist, and patterned by lithography techniques

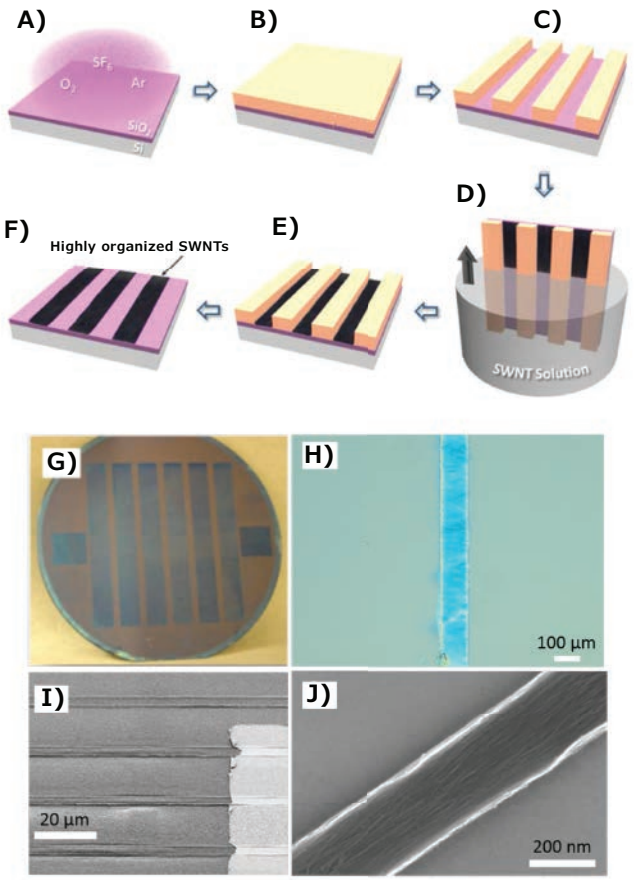

Figure 1. Schematic of template-assisted fluidic SWCNT assembly and SEM image of SWCNT networks. **A**) Surface treatment of SiO_2 substrate by plasma etching. **B–C**) Photoresist coating and template patterning by lithography. **D–E**) SWCNT strip formation by dip coating and assembled SWCNT strips with photoresist pattern. **F**) Highly organized SWCNT strips after removing the photoresist. **G–H**) Photo image of assembled SWCNT strips on the 3-in. wafer and microscopic image of 100 µm width assembled SWCNT networks. **I–J**) SEM images of 4 µm width and 200 nm width assembled SWCNT networks. From References 14,18, with permission from Springer-Verlag and American Chemical Society.

(photo- and e-beam lithography for micro- and nanoscale patterns, respectively). **Figure 1D** demonstrates that the pre-patterned substrate was first vertically submerged into the SWCNT-deionized (DI) water solution using a dip coater and then gradually lifted from the solution with a constant pulling speed. **Figures 1E** and **1C** show the SWCNT network's patterns formed between the micro/nanoscale trenches and the SWCNT networks on the SiO_2 substrate after removing the photoresist. **Figures 1G–J** show the centimeter-scale, millimeter-scale, microscale, and nanoscale assembled SWCNT networks on the SiO_2/Si substrate.

Optoelectronic Applications-Based SWCNTs and Si Heterojunctions

The development of silicon-based photonic circuit components, such as on-chip sources, modulators, storages, etc., are a promising way to solve the bottleneck of transportation speed and integration of conventional silicon circuits.[19,20] Here we show that the highly integrated and controlled heterojunction of SWCNT and silicon can demonstrate a radically unconventional, sharply nonlinear, reverse-bias-dependent photocurrent. This novel phenomenon provides a new way in which to obtain multifunction analog and mixed digital optoelectronic operations with high switching ratios. Large switching of photocurrent can be obtained with small changes in voltage, enabling optoelectronic gate/devices with logic outputs depending on the logic state of both optical and electronic inputs. We demonstrate a number of novel optoelectronic switches/devices and lithographic assembly of a large array of SWCNT architecture devices over a centimeter-scale wafer. **Figures 2A** and **2E** show the schematic and digital photograph of high-density SWCNT-Si heterojunction patterns. The SWCNTs were assembled as micro/nanoscale device architectures on the lightly p-doped silicon surface using the template fluidic method followed by the conventional photolithography, which is shown in **Figure 2F**. **Figure 2B** presents the dark and illuminated I–V curves of SWCNT-Si junctions, and the photocurrent response in a metal-silicon junction with similar dimensions. Though the dark I–V in the SWCNT-Si junctions follows conventional diode rectification behavior, the current clearly deviates from the conventional behavior that sharply rises by several orders of magnitude within a few volts of reverse bias V_r, which is different from the illuminated I–V of a conventional metal-Si Schottky junction with comparable dimension under the same light source. A proposed semi-quantitative model of the band structure of these heterojunctions reveals that the sharply nonlinear photocurrent behavior is possibly related to the reverse-bias-tunable total number of available states in the SWCNT belts, n(ε=eVr). **Figure 2C** presents photographs of an array of SWCNT assembly Si sensors. **Figure 2G** shows interdigitated SWCNT networks connected to source and drain electrodes, which is equivalent to two back-to-back photodiodes forming a bidirectional phototransistor. **Figure 2H** shows a mixed-input optoelectronic AND gate, the light and the applied voltage are the inputs and the measured current is the output. In addition, **Figures 2I–J** show the 2-bit and 4-bit digital optical input, voltage-switchable analog output ADDER circuit separately; when the reversed voltage is applied, the output shows an analog equivalent of digital sum. Hence, SWCNT-Si junctions are a versatile platform for optoelectronic applications ranging from photosensor, photoconvertor, photometry, and imaging.

High-Performance H_2S Detector with SWCNT Devices

SWCNT is the subject of active research for various chemical sensors due to its many advantages, such as unique nanostructure, high mobility, high current density, highly effective electrochemical surface area, etc.[8] Since the pristine CNT-based chemical sensors only utilize their intrinsic electrochemical properties to overcome their limitations in selectivity and sensitivity, functionalizing SWCNTs with covalent or non-covalent materials has been used to further improve the sensitivity of SWCNT-based chemical sensors. Due to its one-dimensional nanostructure, SWCNT is very sensitive to environmental changes such as humidity and surrounding temperature.

In developing a H_2S gas sensor, we used molecular doping of TEMPO as a catalyst on the surface of SWCNTs to improve the sensitivity of H_2S detection by a redox reaction at room temperature. **Figures 3A–D** show the SEM images of highly organized micro-sensor devices from which large scale SWCNT network patterns were fabricated by the template-guided fluidic assembly method, followed by TEMPO coating. **Figure 3E** shows the chemical structure of TEMPO used to functionalize SWCNTs. This compound is capable of oxidizing the gaseous H_2S and can be utilized as a sensory molecule for a H_2S sensor. **Figure 3F** shows the real-time current change of functionalized SWCNT sensor with various concentrations of H_2S gas. **Figure 3G** shows the intrinsic sensitivity of the device and benefits after TEMPO functionalization. Based on our results, TEMPO can be oxidized to $TEMPO^+$, which is a very important product for H2S dissociation. The reduction reaction of $TEMPO^+$ to TEMPO-H is coupled to the dissociation process of H_2S to $S+2H^++2e^-$, since in the air, the SWCNT device shows the P-type properties due to oxygen ions (O_2). Newly generated electrons are donated to SWCNTs to make it less a P-type property, which makes the functionalized SWCNTs more sensitive than the bare SWCNTs. In addition, we find that humidity enhances the sensitivity of H_2S by improving the transfer from TEMPO to $TEMPO^+$. Finally, we demonstrate that a SWCNT device functionalized with TEMPO is highly responsive to the H_2S gas with increasing humidity. This is especially true of semi-SWCNTs, which show a very high sensitivity up to 420% at 60% humidity.

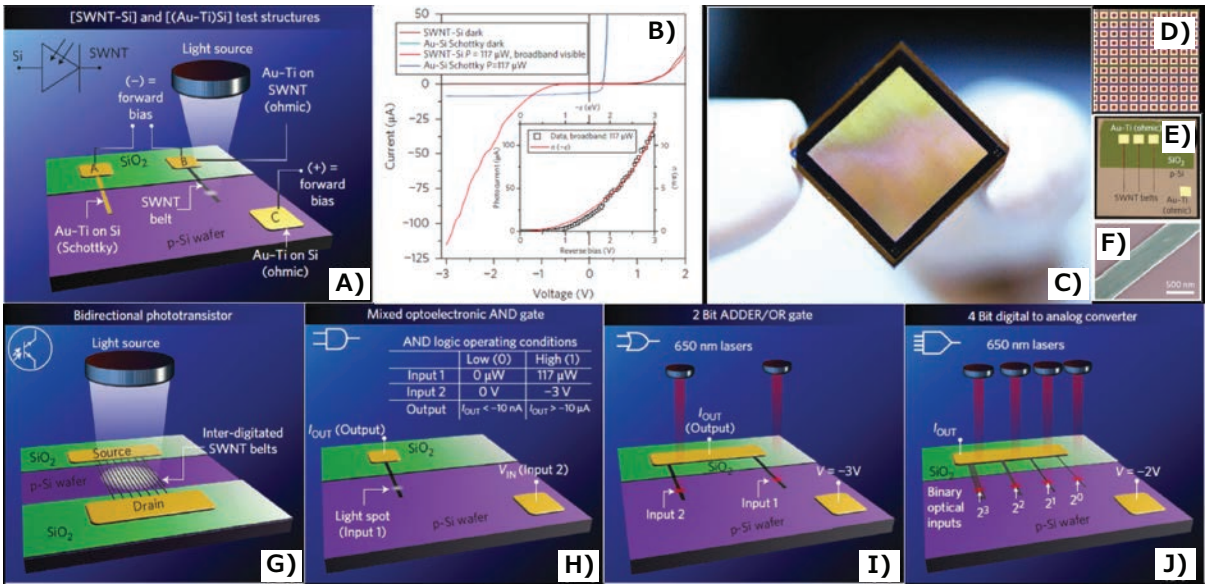

Figure 2. Schematics of novel optoelectronic devices and image of array of SWCNT-Si sensor. **A**) SWCNT-Si heterojunction test structure (2 cm × 2 cm) with electrodes. **B**) Dark and illuminated I–V curves of a typical SWCNT-Si heterojunction **C**) SWCNT-Si sensor: Digital photograph of a 0.25 megapixel array of SWCNT-Si sensors (array area, 12 mm × 12 mm), and **D**) SEM image of the 'core' of the sensor. **E**) Digital photograph of SWCNT-Si heterojunction structure. **F**) SEM image of assembled SWCNT belt. **G**) A bidirectional phototransistor using interdigitated SWCNT fingers attached to source-drain leads. The active region of this device has an area of 3 mm × 200 mm. **H**) An AND gate with optical and electrical inputs and an electrical output. The active region of the junction has an area of 3 mm × 100 mm. Inset table: a typical set of operating conditions determining the 'low' and 'high' logic states for both input and output conditions. **I**) 2-bit ADDER/OR gate with 2 optical inputs and an electrical input and output. **J**) 4-bit digital to analog converter. From Reference 15 with permission from the Nature Publishing Group.

Electrical Fusion of SWCNT Networks: Inter-Allotropic Transformation of Carbon Nanotube Networks

Modifications of sp^2 structured carbon nanotubes usually require extreme and difficult-to-control conditions, such as high temperature, high pressure, and high energy irradiations. Here we present a simple but powerful electrical method to realize the structural transformation of carbon nanotubes from SWCNTs into multiwalled carbon nanotubes (MWCNTs) or multilayer graphene/graphite nanoribbon structures (MGNRs) by applying controlled alternating voltage pulses.

Through controlling the magnitude of the voltage pulse, source-on-time, and the number of switching cycles applied to the SWCNT networks, the targeted transformed nanostructures (MWCNTs or GNRs) can be obtained without the generation of any structural defects. We also find that, after the structure transformation, both electrical conductivity (up to 35% resistance drop) and thermal conductivity (up to 6–7 times higher thermal conductivity, 300 W/mK) of SWCNT networks are greatly improved. **Figure 4A** shows the assembled SWCNT network structure on the TEM grid with metal electrodes. **Figure 4B** shows the I–V curve of SWCNT networks, the maximum current density, and breakdown voltage (V_b). **Figure 4C** shows the time-dependent alternating voltage pulse applied on the SWCNT device. **Figures 4D–F** show the TEM images of pristine SWCNTs, MWNTs ($0.6V_b$, 3,000 cycles), and GNRs ($0.8V_b$, 3,000 cycles) after the electrical fusion process. **Figures 4G–H** show the resistance change and thermal conductivity of SWCNT devices at various applied voltages at the same 3,000 cycles.

Conclusions

We presented, in this article, the template-guided fluidic assembly of highly organized SWCNT networks. Using lithographically patterned template-assisted dip-coating methods, SWCNTs are directly assembled between pre-designed micro- and nanoscale photoresist channels forming densely packed organized SWCNT lateral networks in diverse geometries with feature sizes ranging from 150 nm to several hundred microscales. These highly organized micro- and nanoscale SWCNT network structures can be integrated into a variety of sensing device architectures. The room temperature and wafer-level scaling compatibility of the template-guided fluidic assembly technique provide robust and reproducible device results over large areas. In this regard, we demonstrated a high-performance photodetector and a new kind of logic device using scalable heterojunctions of SWCNTs and silicon, whose output currents can be manipulated completely by both optical and electrical inputs. We also introduced a SWCNT-based chemical sensor which can detect H_2S gas effectively by the redox reactions occurring on SWCNT networks functionalized with TEMPO as a catalyst.

Finally, we demonstrated precisely controlled and well-defined allotropic transformations and formation of their molecular junctions over a large area of SWCNT networks using controlled alternating voltage pulses. Using this newly developed electrical process, small-diameter SWCNTs can be selectively transformed into other allotropic sp^2 nanostructures such as multiwalled carbon nanotubes, multilayered graphene nanoribbons, and structures with sp^3 bonds.

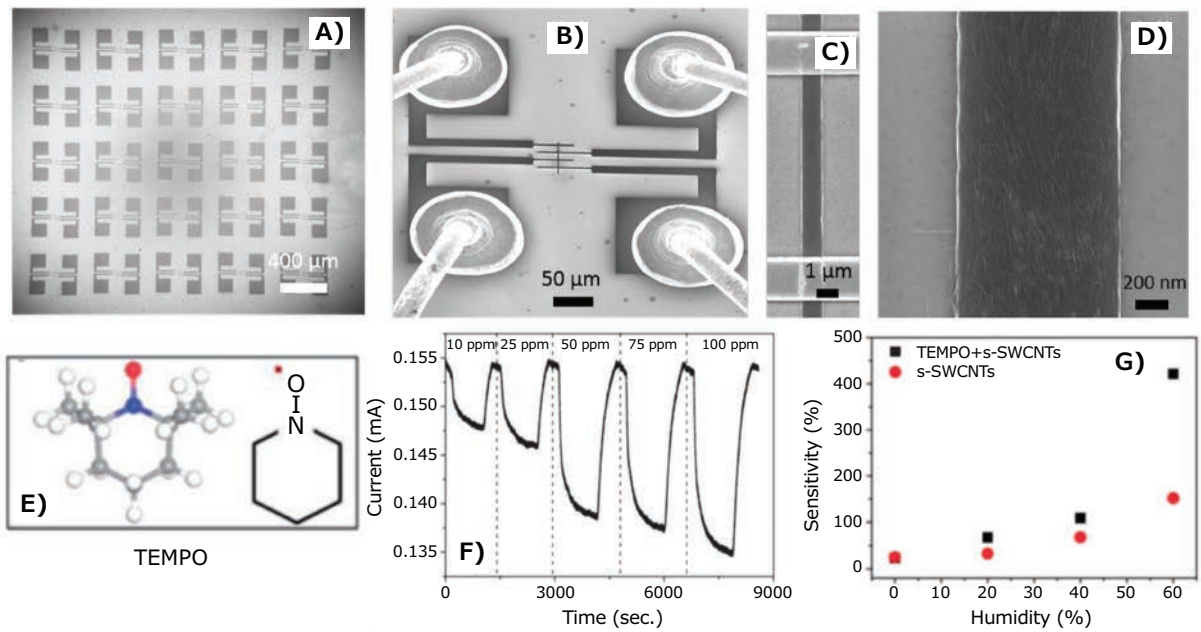

Figure 3. High-performance H2S detector based on SWCNT networks. **A–D**) SEM image of an array of assembled SWCNT devices. **E**) Chemical structure of TEMPO molecules. **F**) Real-time current changes as a function of concentration of H_2S gas for the functionalized SWCNT sensor. **G**) Sensitivity of bare semi-SWCNT device and TEMPO-functionalized SWCNT device as a function of humidity. From Reference 16 with permission from The Royal Society of Chemistry.

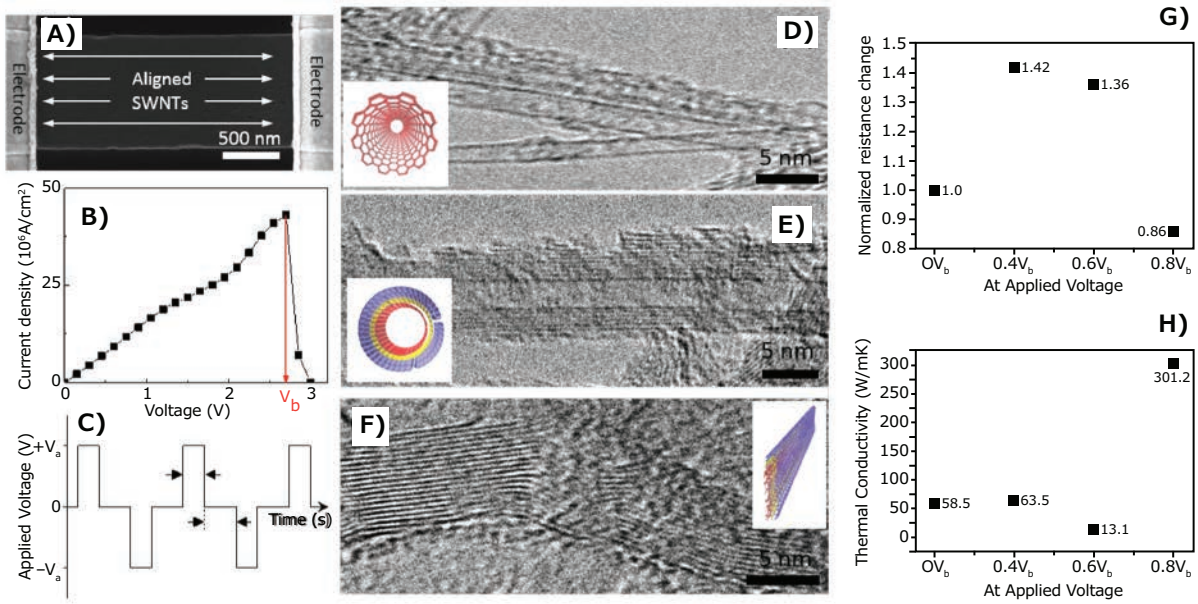

Figure 4. Pulsed alternating voltage-induced allotropic transformation of SWCNT and electrical and thermal properties. **A**) SEM image of an assembled SWCNT network integrated with electrodes fabricated on a specially designed TEM grid. **B**) Typical I-V characteristics of a pristine SWCNT network device showing electrical breakdown behavior, V_b is the breakdown voltage. **C**) Time-dependent alternating voltage pulses that were used for structure transformation of a SWCNT network. **D**) TEM images of pristine SWCNTs. **E**) TEM image of multiwalled structure after applied voltage, $V_a=0.6V_b$ with 3,000 cycling times. **F**) TEM image of multilayer graphite nanoribbons after the network was subjected to 3,000 cycles of $V_a=0.8V_b$. **G–H**) Electrical and thermal properties of SWCNT networks at various applied voltages at 3,000 cycling times. From Reference 17 with permission from Nature Publishing Group.

References

(1) Iijima, S. *Nature* **1991**, *354*(6348), 56–58.
(2) Avouris, P. *Acc. Chem. Res*. **2002**, *35*(12), 1026–1034.
(3) Dai, H. *Acc. Chem. Res*. **2002**, *35*(12), 1035–1044.
(4) Yao, Z.; Kane, C. L.; Dekker, C. *Phys. Rev. Lett*. **2000**, *84*(13), 2941–2944.
(5) White, C. T.; Todorov, T. N. *Nature* **1998**, *393*(6682), 240–242.
(6) Pop, E.; Mann, D.; Wang, Q.; Goodson, K.; Dai, H. *Nano Lett*. **2006**, *6*(1), 96–100.
(7) Lu, J. P. *J. Phys. Chem. Solids* **1997**, *58*(11), 1649–1652.
(8) Kong, J.; Franklin, N. R.; Zhou, C.; Chapline, M. G.; Peng, S.; Cho, K.; Dai, H. *Science* **2000**, *287*(5453), 622–625.
(9) Wen, L.; Li, F.; Cheng, H.-M. *Adv. Mater*. **2016**, *28*(22), 4306–4337.
(10) Fan, S.; Chapline, M. G.; Franklin, N. R.; Tombler, T. W.; Cassell, A. M.; Dai, H. *Science* **1999**, *283*(5401), 512–514.
(11) Kam, N. W. S.; O'Connell, M.; Wisdom, J. A.; Dai, H. *Proc. Natl. Acad. Sci. U.S.A*. **2005**, *102*(33), 11600–11605.
(12) Jaber-Ansari, L.; Hahm, M. G.; Somu, S.; Sanz, Y. E.; Busnaina, A.; Jung, Y. J. *J. Ame. Chem. Soc*. **2009**, *131*(2), 804–808.
(13) Xugang, X.; Chia-Ling, C.; Peter, R.; Ahmed, A. B.; Yung Joon, J.; Mehmet, R. D. *Nanotech*. **2009**, *20*(29), 295302.
(14) Jaber-Ansari, L.; Hahm, M. G.; Kim, T. H.; Somu, S.; Busnaina, A.; Jung, Y. J. *App. Phys. A* **2009**, *96*(2), 373–377.
(15) Kim, Y. L.; Jung, H. Y.; Park, S.; Li, B.; Liu, F.; Hao, J.; Kwon, Y.-K.; Jung, Y. J.; Kar, S. *Nat. Photon*. **2014**, *8*(3), 239–243.
(16) Jung, H. Y.; Kim, Y. L.; Park, S.; Datar, A.; Lee, H.-J.; Huang, J.; Somu, S.; Busnaina, A.; Jung, Y. J.; Kwon, Y.-K. *Analyst* **2013**, *138*(23), 7206–7211.
(17) Jung, H. Y.; Araujo, P. T.; Kim, Y. L.; Jung, S. M.; Jia, X.; Hong, S.; Ahn, C. W.; Kong, J.; Dresselhaus, M. S.; Kar, S.; Jung, Y. J. *Nat. Comm*. **2014**, *5*, 4941.
(18) Kim, Y. L.; Li, B.; An, X.; Hahm, M. G.; Chen, L.; Washington, M.; Ajayan, P. M.; Nayak, S. K.; Busnaina, A.; Kar, S.; Jung, Y. J. *ACS Nano*. **2009**, *3*(9), 2818–2826.
(19) Almeida, V. R.; Barrios, C. A.; Panepucci, R. R.; Lipson, M. *Nature* **2004**, *431*(7012), 1081–1084.
(20) Liu, L.; Kumar, R.; Huybrechts, K.; Spuesens, T.; Roelkens, G.; Geluk, E.-J.; de Vries, T.; Regreny, P.; Van Thourhout, D.; Baets, R.; Morthier, G. *Nat. Photon*. **2010**, *4*(3), 182–187.

Carbon Nanomaterials

For a complete list of available materials, visit **SigmaAldrich.com/cnt**.

Single-Walled Carbon Nanotubes

Production Method	Dimensions	Purity	Prod. No.
CoMoCAT™ Catalytic Chemical Vapor Deposition (CVD) Method	diameter 0.6 - 1.1 nm	>95% (carbon as SWCNT)	**775533-250MG** **775533-1G**
	diameter 0.7 - 1.4 nm	≥80.0% (carbon as SWNT)	**724777-250MG** **724777-1G**
	diameter 0.7 - 1.3 nm L 450-2300 nm (mode: 800nm; AFM)	≥70% (carbon as SWNT)	**704113-250MG** **704113-1G**
Catalytic Carbon Vapor Deposition (CCVD) Method	average diameter 2 nm several microns (TEM)	>70%	**755710-250MG** **755710-1G**
Electric Arc Discharge Method	diameter 1.2 - 1.7 nm L 0.3-5 µm	30% (Metallic) 70% (Semiconducting)	**750492-100MG**
	diameter 1.2 - 1.7 nm L 0.3-5 µm	30% (Metallic) 70% (Semiconducting)	**750514-25MG**

Single-Walled Carbon Nanotube Inks

SWCNT Concentration	Form	Viscosity	Sheet Resistance	Prod. No.
1.00 +/- 0.05 g/L (SWCNT concentration by Absorbance at 854 nm)	dispersion in H_2O (black liquid)	3.0 mPa.s (at 10 sec^{-1} shear rate)	<600 Ω/sq (at 85% VLT (ohm/square), by 4-point probe on prepared film by rod coating)	**791504-25ML** **791504-100ML**
1 mg/mL	viscous liquid (black)	17.7 Pa.s at 25 °C (at 10 sec^{-1} shear rate)	<1000 Ω/sq (by 4-point probe on prepared, at 87.5% VLT (ohm/sq))	**792462-25ML** **792462-100ML**
0.20 +/- 0.01 g/L (by Absorbance at 854 nm)	dispersion in H_2O (black liquid)	~1.0 mPa.s	<400 Ω/sq (by 4-point probe on prepared film by spray)	**791490-25ML** **791490-100ML**

Double-Walled Carbon Nanotubes

Production Method	Dimensions	Purity	Prod. No.
Catalytic Carbon Vapor Deposition (CCVD) Method	avg. diam. × L 3.5 nm × >3 µm (TEM)	Metal Oxide ≤10% TGA	**755141-1G**
	avg. diam. × L 3.5 nm × 1-10 µm (TEM)	Metal Oxide <10% TGA	**755168-1G**
Chemical Vapor Deposition (CVD) Method	O.D. × I.D. × L 5 nm × 1.3-2.0 nm × 50 µm	50-80%	**637351-250MG** **637351-1G**

Multi-Walled Carbon Nanotubes

Production Method	Description	Purity	Prod. No.
Catalytic Carbon Vapor Deposition (CCVD) Method	avg. diam. × L 9.5 nm × <1 µm (TEM) thin and short	Metal Oxide <5% TGA	**755117-1G**
	avg. diam. × L 9.5 nm × 1.5 µm (TEM) thin	Metal Oxide <5% TGA	**755133-5G**
Chemical Vapor Deposition (CVD) Method	O.D. × L 6-13 nm × 2.5-20 µm 12 nm (average diameter, HRTEM) 10 µm (average length, TEM)	>98% carbon basis	**698849-1G**
	D × L 110-170 nm × 5-9 µm	>90% carbon basis	**659258-2G** **659258-10G**
Electric Arc Discharge Method	O.D. × L 7-12 nm × 0.5-10 µm powdered cylinder cores	20-30% MWCNT basis	**406074-500MG** **406074-1G** **406074-5G**
	O.D. × L 7-15 nm × 0.5-10 µm as-produced cathode deposit	>7.5% MWCNT basis	**412988-100MG** **412988-2G** **412988-10G**

Carbon Nanohorns

Purity	Diameter	Surface Area (BET)	Prod. No.
90%, TGA	2-5 nm (TEM)	1300-1400 m^2/g	**804126-250MG**
90%, TGA	2-5 nm (TEM)	400 m^2/g	**804118-250MG**

Graphene Nanoribbons

For a complete list of available materials, visit **SigmaAldrich.com/graphene**.

Name,	Purity	Dimension (L x W)	Surface Area (BET)	Prod. No.
Graphene nanoribbons, alkyl functionalized	≥85% carbon basis, TGA	2-15 µm × 40-250 nm	38 m^2/g	**797766-500MG**
Graphene nanoribbons	≥90.0% carbon basis, TGA	2-15 µm × 40-250 nm	48-58 m^2/g	**797774-500MG**

Substrates

Silicon Wafers (single side polished, cubic (a = 5.4037))

For a complete list of available materials, visit **SigmaAldrich.com/si-wafer**.

Type	Orientation	Dimension (diam. x thickness)	Dopant	Prod. No.
N-type	<100>	2 in. × 0.5 mm	No	**646687-1EA** **646687-5EA**
	<100>	3 in. × 0.5 mm	No	**647535-1EA** **647535-5EA**
	<100>	2 in. × 0.5 mm	phosphorus	**647780-1EA** **647780-5EA**
	<100>	3 in. × 0.5 mm	phosphorus	**647802-1EA**
P-type	<100>	2 in. × 0.5 mm	boron	**647675-5EA** **647675-1EA**
	<100>	3 in. × 0.5 mm	boron	**647764-1EA**

Type	Orientation	Dimension (diam. x thickness)	Dopant	Prod. No.
N-type	<111>	2 in. × 0.5 mm	No	**647101-1EA** **647101-5EA**
	<111>	3 in. × 0.5 mm	No	**647543-1EA** **647543-5EA**
	<111>	2 in. × 0.5 mm	phosphorus	**647799-1EA** **647799-5EA**
P-type	<111>	2 in. × 0.3 mm	boron	**647705-1EA**
	<111>	3 in. × 0.5 mm	boron	**647772-5EA**

Single Crystal Substrates

For a complete list of available materials, visit **SigmaAldrich.com/singlecrystal**.

Name	Composition	Dimensions	Orientation	Prod. No.
Aluminum oxide	Al_2O_3	L × W × thickness 10 × 10 × 0.5 mm	<0001>	**634875-1EA** **634875-5EA**
Gallium antimonide	GaSb	diam. × thickness 2 in. × 0.5 mm	<100>	**651478-1EA**
Gallium arsenide	GaAs	diam. × thickness 2 in. × 0.5 mm	<100>	**651486-1EA**
Gallium phosphide	GaP	diam. × thickness 2 in. × 0.5 mm	<111>	**651494-1EA**
Lanthanum aluminum oxide	$LaAlO_3$	10 × 10 × 0.5 mm	<100>	**634735-1EA**
LSAT	$(LaAlO_3)_3(Sr_2AlTaO_6)_7$	10 × 10 × 0.5 mm	<100>	**635050-1EA**
Magnesium aluminate	$MgO·Al_2O_3$	L × W × thickness 10 × 10 × 0.5 mm	<100>	**635073-1EA**
	$MgO·Al_2O_3$	10 × 10 × 0.5 mm	<110>	**634840-1EA**
	$MgO·Al_2O_3$	10 × 10 × 0.5 mm	<111>	**634832-1EA**
Magnesium oxide	MgO	L × W × thickness 10 × 10 × 0.5 mm	<100>	**634646-1EA**
	MgO	L × W × thickness 10 × 10 × 0.5 mm	<111>	**634697-1EA**
Silicon dioxide	SiO_2	L × W × thickness 10 × 10 × 0.5 mm	<0001>	**634867-5EA**
Strontium titanate	$SrTiO_3$	10 × 10 × 0.5 mm	<111>	**638161-1EA**
	$SrTiO_3$	10 × 10 × 0.5 mm	<100>	**634689-1EA**
Titanium(IV) oxide, rutile	TiO_2	L × W × thickness 10 × 10 × 0.5 mm	<001>	**635057-1EA**
	TiO_2	L × W × thickness 10 × 10 × 0.5 mm	<100>	**635049-1EA**
	TiO_2	L × W × thickness 10 × 10 × 0.5 mm	<110>	**635065-1EA**

MilliporeSigma

it's elemental

Goodfellow Alloys and Pure Elements

High-purity metals and alloys play an essential role in applications such as biomedical engineering and physical vapor deposition. Advances in materials science require materials that ensure optimum properties, performance, and quality. Over 9,900 elemental materials and 7,800 alloys are now available from Goodfellow Cambridge Ltd., a leading international supplier of metals and materials for research and industry.

Materials innovation requires the correct composition and physical form. Choose from:

- Foils
- Rods
- Wires
- Tubes
- Fibers
- Bars
- Sheets
- Foams
- Honeycombs
- Spheres
- Powders
- Meshes

For a full selection of ultra-high purity materials, visit **go.SigmaAldrich.com/itselemental**

Representative Materials

Name	Dimensions	Specifications	Prod. No.
Aluminum-Lithium-Copper Alloy	OD 24 mm; ID 22 mm	99% purity	**GF55446295**
Carbon, Fiber	0.007 mm diameter	Tex number 200, 3,000 filaments	**GF20790558**
Iron-Nickel Alloy	45 micron powder	99.9% purity	**GF59815435**
Tantalum, Tube	OD 0.31 mm; ID 0.19 mm	Trace metal purity, 99.9%	**GF33615716**
Niobium, Insulated Wire	0.125 mm diameter	Insulated wire, polyimide insulation	**GF76912308**
Ytterbium, Foil	0.80 mm, 60 × 60 mm	99% purity	**GF14565865**

GoodFellow

Synthesis of Gold Nanorods: Avoiding Common Pitfalls



Brantley C. Henson, Justin T. Harris, Kimberly A. Homan*

NanoHybrids Inc.
3913 Todd Ln #310, Austin, TX 78744, USA
*Email: kimberly.homan@nanohybrids.net

Introduction

Plasmonic nanoparticles have unique optical properties that can be tailored to suit a variety of applications in the biotechnology[1-8] and electronics[9-16] industries. Gold nanorods (**Figure 1**), a particular subset of plasmonic nanoparticles, are of interest for biomedical applications due to their tunability in the near-infrared (NIR) light spectrum and biological inertness.[17-20] There are numerous techniques for the synthesis of gold nanorods, including templating,[21-25] electrochemical growth,[26-28] and reverse micellar systems.[29-30] Here, we focus on seed-mediated colloidal growth methods. While there are multiple published variations on the seed-mediated colloidal growth of gold nanorods,[29,31-38] our discussion will examine the well-known approaches pioneered by Nikoobakht and Murphy.[31,39] Seed-mediated colloidal growth has many advantages over the aforementioned methods,[41] including no need for specialized equipment and straightforward scalability—eventual requirements for clinical translation.[43-44] Although these methods are well understood, their sensitivity to small changes in reaction conditions can lead to a lack of control over the size, shape, purity, and aspect ratio of rods from batch to batch.[19,33,36-37,44-50] In this review, we briefly discuss seed-mediated gold nanorod synthesis, and then present a detailed discussion of the common pitfalls and how best to avoid them.

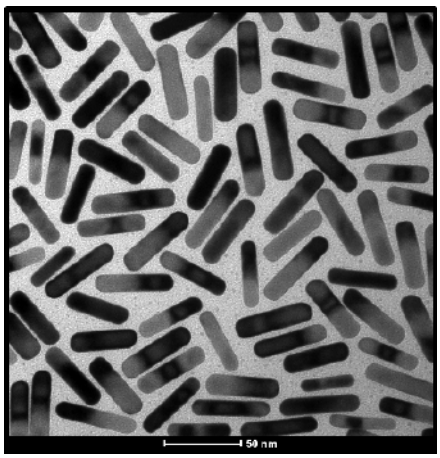

Figure 1. TEM image of typical gold nanorods.

Synthesis

Basic synthesis follows the work of Nikoobakht and Murphy,[31,37,39,51-52] where precise reactant concentrations and volumes are discussed. Briefly, a growth solution composed of cetyltrimethylammonium bromide (CTAB, **Prod. No. 52370**), water, silver nitrate ($AgNO_3$, **Prod. No. 792276**), and chloroauric acid ($HAuCl_4$, **Prod. No. 254169**) is prepared. If a multisurfactant system is required for longer aspect ratios, benzyldimethyl ammonium chloride (BDAC) is also typically included, though other surfactants such as sodium oleate (**Prod. No. O7501**) have also been reported.[46,53] Ascorbic acid (**Prod. No. A92902**) is then added to reduce the Au^{3+} to Au^{1+}. To template further reduction of gold, small gold nanoparticle seeds are then added to the solution. The seeds are synthesized via a rapid reduction of $HAuCl_4$ by sodium borohydride (**Prod. No. 480886**) in a CTAB or citrate solution. Upon addition of the seeds, Au^{1+} is further reduced to metallic Au^0, with the surfactants and Ag serving to break the symmetry through preferential deposition on the {110} facets of gold, inhibiting growth[54] and encouraging growth parallel to the {001} plane, resulting in anisotropic gold nanorods.[31]

Six Common Pitfalls in Gold Nanorod Synthesis

The Importance of Good Synthesis Preparation (1)

Slight adjustments in overall concentrations, impurities, and nucleation sites can result in significant differences in particle size, shape, and purity, rendering reproducibility a concern. Thus, successful and repeatable gold nanorod synthesis is highly reliant upon proper and consistent preparation and lab technique. First, to ensure even growth, nucleation sites must be well controlled. As a general requirement for most metallic nanoparticle syntheses, all glassware and stir bars must be thoroughly cleaned with aqua regia[55] to remove residual metals. Any residual metal will lead to unwanted pre-nucleation in the growth solution, making controlled synthesis impossible. All water used throughout the synthesis process, including glassware cleaning, needs to be 18.2 MΩ·cm ASTM Type I water (commonly referred to as deionized ultrafiltrated, DIUF, or "Nanopure™" water). Likewise, the lab space should be clean, with minimal dust.

Another common cause of variability from lab to lab, or even person to person, is the reagent preparation; even when buying from the same supplier, minor changes in impurities from lot to lot can affect the final product of the nanorod synthesis. For example, Korgel et al. report on the effect of the CTAB source on nanorod synthesis.[33] Interestingly, the results indicate trace impurities in CTAB, particularly iodine, are actually required in order to produce high quality rods.[56] Similarly, NanoHybrids has found changing the gold acid source can affect the overall size and longitudinal surface plasmon resonance (LSPR) of the resulting rods. For these reasons, documentation and tracking of reagents is necessary for all synthesis. Whenever changing reagent lots or sources, pilot reactions should first be performed to set the new baseline for further size and shape tuning. Other considerations include reagent age and storage conditions. For ease of reaction and to minimize inherent weighing errors, many groups choose to make stock solutions of reactants. Recent work by Murphy et al.[38] demonstrated solutions of silver nitrate and ascorbic acid are best prepared fresh due to their susceptibility to photodegradation. Likewise, the age of CTAB solutions has been shown to affect the final product.[38] Depending on the quantity and scale of reactions a lab produces, these effects can either be detrimental or potentially leveraged for increased control over reaction kinetics. Again, proper documentation is paramount to success.

Aggregation Happens: Rod Instability (2)

One of the most common problems during synthesis is nanoparticle aggregation. Knowing when aggregation occurs is just as important as knowing how to prevent it. Aggregation of nanorods with an absorbance in the NIR spectrum can be easily detected by ultraviolet-to-visible (UV/Vis) spectrophotometry. The main indication of aggregation is the presence of a "shoulder" in the extinction spectra. A typical "good" spectrum is shown in **Figure 2A**. Note the high ratio of the LSPR peak to the transverse surface plasmon resonance (TSPR) peak (labeled as L/T, **Figure 2A**), and the narrow, symmetric shape of the LSPR peak. **Figure 2B** shows the result of slight aggregation. Note the obvious lack of symmetry and right-side skew of the LSPR band caused by plasmon coupling in gold nanorod aggregates. Similarly, **Figure 2C** shows particles made with a dual surfactant system (CTAB + BDAC). While not as obvious as **Figure 2B**, the asymmetry of the LSPR band and increased full width half maximum (FWHM) indicates problems with the synthesis, such as high polydispersity of size and aspect ratio or slight aggregation. These problems are not inherent to all dual-surfactant reactions and, thus, is an indicator of a failed reaction. Also, note the shape of the TSPR band (BDAC Trans Peak) in **Figure 2C**. The additional small shoulder is due to subtle differences in the shape of the rods themselves, along with the associated impurities (cubes vs. spheres). Even in a "good" dual-surfactant reaction with a narrow LSPR and high symmetry, this variation in the TSPR band is expected. A spectrum of nanorods with high amounts of shape impurities (large numbers of spheres and cubes) is shown in **Figure 2D** and discussed further in pitfall #4. Finally, severe aggregation can be easily identified by particle precipitation or a change in appearance from various shades of red to dark gray or purple, such as in **Figure 2E**.

The root cause of aggregation is often difficult to identify due to the complexity of the synthesis. Unexpected impurities in new reagents, reagent aging, incompatible reagent combinations, contamination, and improper product purification (discussed later) are all potential sources of the problem. To mitigate these problems and maintain general synthesis consistency, it is recommended that regular small-scale pilot studies (20–30 mL reactions) be performed on a monthly to quarterly

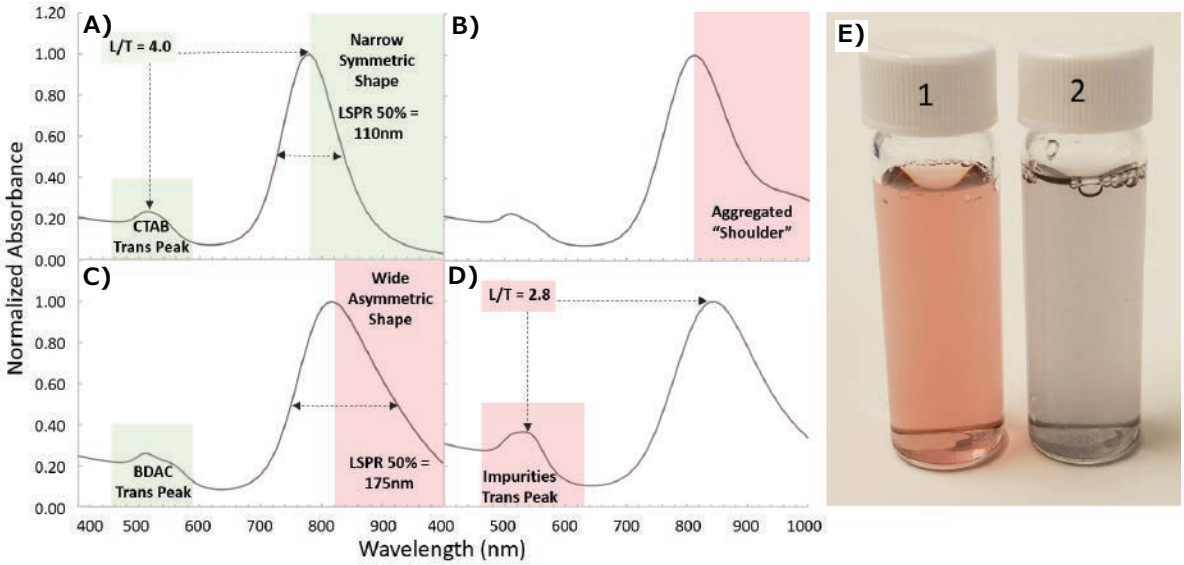

Figure 2. Spotting nanorod aggregation and shape impurities using normalized UV/Vis spectra. **A**) Ideal spectra of gold nanorods synthesized with a single surfactant (CTAB) is evidenced by a high LSPR/TSPR peak ratio (L/T) and a narrow symmetric LSPR peak. **B**) Spectra displaying aggregates in a "shoulder." **C**) Spectra of particles synthesized in a binary surfactant (CTAB and BDAC) is shown by the shape of the transverse peak. The spectrum contains a wide asymmetric LSPR peak indicating wide size distribution. **D**) Spectra of particles exhibiting high amounts of shape impurities. **E**) Photo of (1) as-synthesized and (2) aggregated gold nanorods.

basis to verify the quality of reagents and identify sources of contamination or degradation. It is important to note that while small-scale reactions are used for verification purposes and reproducibility in comparison to previous studies, the exact peak absorption typically shifts when the reaction is conducted at a larger scale; specifically, a lower LSPR is expected upon scale-up. Moreover, the actual resultant peak is also dependent upon vessel size, shape, spin speed, and heating efficiency. As a result, the expected LSPR shift should be determined for any new glassware and protocol for consistent targeting of LSPR wavelengths.

Poor Control Over Aspect Ratio (3)

One of the unique properties of gold nanorods is the tunability of their optical peak absorption from the visible to IR range simply by changing their aspect ratio (defined as the ratio between length and width/diameter of the nanorod). Within the standard seed-mediated growth protocols, this requires breaking the symmetrical growth, which is thermodynamically favored, to encourage growth along a single axis. To this end, silver nitrate is a reliable tool for lengthening gold nanorods.[31] As seen in **Figure 3A**, generally increasing the silver nitrate concentration increases the aspect ratio and corresponding LSPR, but this method only works up to ~850 nm. For aspect ratios greater than 4.5 or an LSPR greater than 850 nm, Nikoobahkt demonstrated that varying the ratio of BDAC and CTAB in a binary surfactant system yields aspect ratios up to 10 (**Figure 3B**).[31] Values as high as 70 have been reported by implementing a multistage addition of growth solution to seeds, as reported by Murphy et al.[57] Perez-Marzan demonstrated a correlation between increased seed amount and decreased aspect ratio.[58] Whichever approach is chosen, the delicate interplay within the multivariable synthetic system illustrates the importance of tight control over the reactant concentrations while making it possible to synthesize a wide range of high quality gold nanorods (**Figure 3D**). For consistency, massing your reactants versus relying on volumetric techniques is recommended.

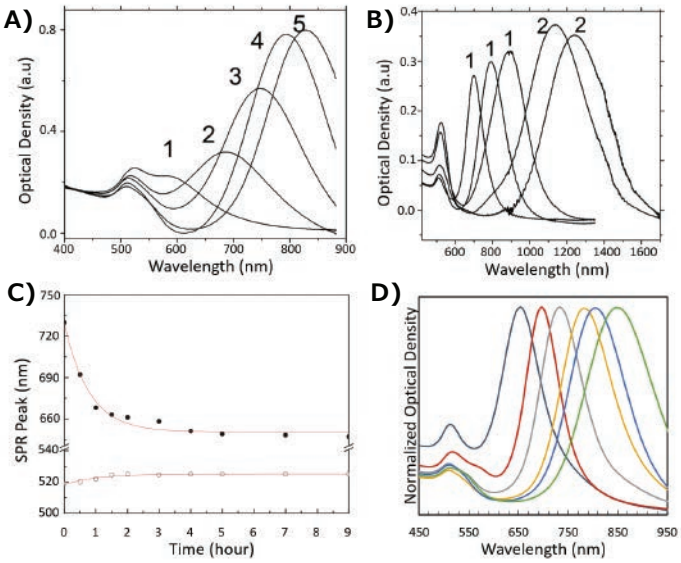

Figure 3. Controlling the aspect ratio of gold nanorods. **A**) Effect of increasing silver nitrate concentration on the nanorod aspect ratio and resulting optical properties upon synthesis. (1–5) indicate increasing additions of 4 mM $AgNO_3$ from 50–300 µL to identical growth solutions.[31] **B**) The effect of using single (1) and binary (2) surfactant systems in the synthesis of gold nanorods.[31] **C**) The effect of heating on the LSPR peak (closed dots) and TSPR peak (open dots) of aqueous solutions of gold nanorods.[42] **D**) An array of nanorods synthesized using combinations of tuning reactions discussed.

It is also worth considering that in all syntheses involving gold nanorods, there is a tendency for the nanorod aspect ratio to decrease over time, which will cause a blue-shift in the LSPR peak. This blue-shift is thought to be a consequence of Ostwald ripening, via a softening of any sharp edges to a more thermodynamically stable arrangement.[42] You can, therefore, artificially speed up the rate of Ostwald ripening by thermal treatment of the particles in an aqueous solution, lowering their aspect ratio (**Figure 3C**).

Poor Shape Control (4)

During any nanorod synthesis, the appearance of shape impurities is inevitable. However, these impurities can be monitored and minimized. **Figure 2D** illustrates a nanorod reaction with poor shape purity. Unwanted spheres in the reaction have a strong absorbance at 510–525 nm, resulting in an increase in the apparent TSPR peak. Thus, monitoring the LSPR/TSPR ratio is a strong indicator of overall shape purity. A "good" ratio of at least 3.5 indicates ~90% shape purity.[59-60] If a high quantity of impurities is observed, this can indicate that reactants are too old, not enough $AgNO_3$ was used in the reaction, reaction temperature was too high, or too high of a BDAC/CTAB ratio was used, to name a few potential problems. Post-synthesis separations can be performed to remove unwanted shapes, as discussed in the next section. Likewise, several variations of the basic cylindrical shape of nanorods can emerge during their synthesis. Binary surfactant reactions such as those using both BDAC and CTAB generate rods with sharper corners, giving them a more "brick-like" structure (**Figure 4A**) versus the standard CTAB reaction (**Figure 4B**). Spectrally, this can be observed as an additional small peak slightly red-shifted from the typical TSPR peak (**Figure 2A vs 2C**). "Dog bones" or "dumbbells" are another feature that can dramatically affect the spectra of nanorods (**Figure 4C**). Several groups report these features appear upon secondary additions of ascorbic acid and

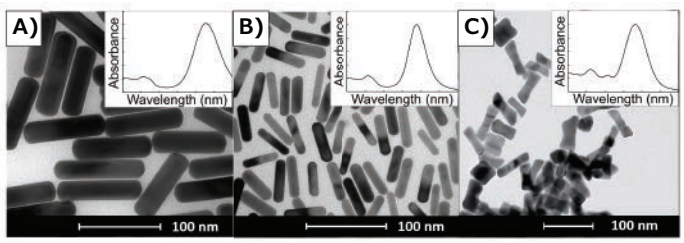

Figure 4. TEMs of gold nanorods demonstrating a correlation between absorbance spectra and anisotropic geometry of gold nanorods. Insets are typical corresponding UV/Vis spectra for the given shape, spanning 400–1,000 nm. **A**) Gold nanorods synthesized in binary surfactant system containing CTAB and BDAC. **B**) Gold nanorods synthesized using only CTAB. **C**) Dog bone- or dumbbell-shaped nanoparticles.[40]

are pH driven.[32,50–51] We have observed these same features via adding excessive ascorbic acid in a single addition. It is possible to "soften" features like sharp corners and dog bones through thermal treatment, resulting in a reduced intensity of their additional spectral features and an overall blue-shift of their LSPR.

Insufficient Purification (5)

After any synthesis, purification is required to remove excess reactants and reduce the overall concentration of CTAB for storage. If left in the original reactants for 48 h or more, nanorods have a tendency to aggregate. Thus, purification is typically accomplished by pelleting via centrifugation, and the main pitfall is aggregation post-centrifugation. Since different sizes of particles will require different spin speeds to adequately drop out of solution, optimization for your particular nanorods is necessary. Centrifuging particles at too high of a speed or for too long can lead to the formation of aggregates, while under-centrifuging results in nanorod losses. This is especially true for nanorods with higher aspect ratios with absorbance outside of the visible spectra. Counterintuitively, higher aspect ratio rods are more stable in solution and, thus, require higher spin speeds for precipitation. Therefore, it is recommended that you check the UV/Vis spectra of supernatants before discarding. It is also important to be mindful of the final concentration of CTAB in your solution, as the removal of too much CTAB can cause the nanorods to become unstable. Typically, we recommend maintaining >10 mM surfactant through all purification steps. Particles can then be safely diluted to 1 mM CTAB for final storage. As seen in **Figure 5**, centrifugation can also be used for additional separation and purification of a sample with high shape impurities. While the majority of particles will remain together in a pellet (3), you can see on the fringes a differentiation in color (1 and 2) indicative of sphere and rod separation. While the method is inefficient, centrifugal separation can be utilized to increase purity and has been reported previously.[61] Other groups have also explored multiphase centrifugal separations[62] and flocculation[63] techniques with some success.

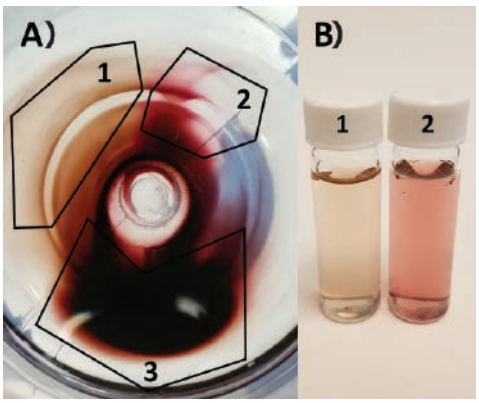

Figure 5. A) Top-down view of centrifuge tube containing gold nanoparticle pellet. Particles partially separate according to size and particle geometry: 1) Very high shape purity nanorod population. 2) Primarily nanosphere population. 3) Mix of both populations. B) Photo of (1) highly purified gold nanorods and (2) primarily spheres from pellet in A).

Incomplete Characterization (6)

In order to properly characterize nanorods, it is important to use multiple complimentary techniques to assess their quality. The most commonly used characterization tools are UV/Vis spectrophotometers, transmission electron microscopy (TEM), scanning electron microscopy (SEM), dynamic light scattering (DLS), and zeta potential. As discussed previously, UV/Vis spectroscopy is the most useful tool for measuring aspect ratio, shape purity, and rod quality for an ensemble of nanoparticles. However, UV/Vis provides little information on actual size. TEM and SEM are the most robust tools for verifying particle dimension, but without taking a proper number of images and doing so at multiple magnifications, it is easy to accidently bias the true average dimension of your particles. **Figure 6** illustrates just how different the quality of a lot of nanorods can look based on what section of a TEM grid you choose to observe.[47] **Figure 6C** demonstrates that particles can have a tendency to "self-sort" when drying on a grid. Groups of impurities such as spheres or cubes can separate from sections of rods leaving the false impression of a high shape purity synthesis.

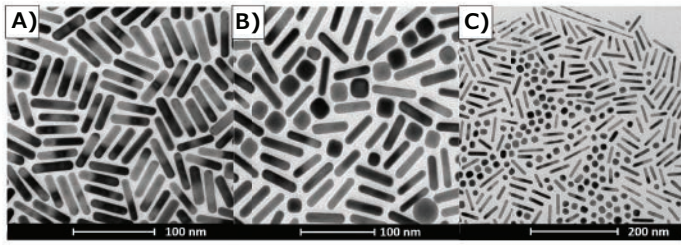

Figure 6. TEM's of gold nanorods illustrating selection bias. A) Section of TEM grid indicates high purity rod synthesis. B) Different section of same grid shown by (A) indicates a large number of impurities in sample. C) TEM demonstrates shape segregation drying pattern on TEM grid.

Techniques such as dynamic light scattering (DLS), which are typically employed for the characterization of spherical nanoparticles, rely on algorithms that are not designed for detection and sizing of nanorods due to their anisotropic geometry. However, measurement of the zeta potential can still act as a good marker of stability for nanorods stabilized by CTAB. Typically, stable as-synthesized gold nanorods after purification have a zeta potential >+30 mV; lower values indicate particle instability and a high likelihood of aggregation with time. Alternatively, gold nanorods can undergo ligand exchanges to be sterically stabilized by neutral moieties, such as polyethylene glycol (PEG). This method is often employed to remove CTAB and reduce particle toxicity, resulting in a zeta potential of ±5 mV.

Conclusions

The synthesis of gold nanorods via colloidal seed-mediated growth offers the user tunability over a wide range of aspect ratios and corresponding LSPR optical peaks, with the opportunity for easy volumetric synthesis scaling. However, this tunability comes at a price; a synthesis that requires precise control over a number of variables in multiple phases of the process. The extensive list of variables leads to difficulty in reproducibility and consistency of reactions, potentially frustrating researchers who are moving toward large-scale *in vivo* studies. Because of these challenges, small-scale manufacture can be costly to maintain.[64] Therefore, many researchers opt to purchase nanorods rather than produce them in-house, as many companies now provide them as products with good quality control and standardized characterization.

References

(1) Lee, K. S.; El-Sayed, M. A. *J. Phys. Chem. B* **2005**, *109* (43), 20331–8.
(2) Jain, P. K.; Huang, X.; El-Sayed, I. H.; El-Sayed, M. A. *Acc. Chem. Res.* **2008**, *41* (12), 1578–86.
(3) Loo, C. H.; Lee, M.-H.; Hirsch, L. R.; West, J. L.; Halas, N. J.; Drezek, R. A. *Proc. SPIE* **2004**, 5327, 1–4.
(4) Huang, X.; El-Sayed, I. H.; Qian, W.; El-Sayed, M. A. *Nano Lett.* **2007**, *7* (6), 1591–1597.
(5) El-Sayed, I. H.; Huang, X.; El-Sayed, M. A. *Cancer Lett.* **2006**, *239* (1), 129–135.
(6) Aslan, K.; Leonenko, Z.; Lakowicz, J. R.; Geddes, C. D. *J. Fluoresc.* **2005**, *15* (5), 643–654.
(7) Aslan, K.; Lakowicz, J. R.; Geddes, C. D. *Curr. Opin. Chem. Biol.* **2005**, *9* (5), 538–544.
(8) Travis, K.; Aaron, J.; Harrison, N.; Sokolov, K. *Plasmonics in Biology and Medicine V*, VoDinh, T.; Lakowicz, J. R., Eds. **2008**; Vol. *6869*, pp H8690–H8690.
(9) Mubeen, S.; Lee, J.; Lee, W. R.; Singh, N.; Stucky, G. D.; Moskovits, M. *ACS Nano* **2014**, *8* (6), 6066.
(10) Moran, C. E.; Steele, J. M.; Halas, N. J. *Nano Lett.* **2004**, *4* (8), 1497–1500.
(11) Maier, S. A.; Brongersma, M. L.; Kik, P. G.; Meltzer, S.; Requicha, A. A. G.; Atwater, H. A. *Adv. Mater.* **2001**, *13* (19), 1501–1505.
(12) Jackson, J. B.; Halas, N. J. *Proc. Natl. Acad. Sci. U.S.A.* **2004**, *101* (52), 17930–17935.
(13) Gryczynski, I.; Malicka, J. B.; Gryczynski, Z.; Nowaczyk, K.; Lakowicz, J. R. *Proc. SPIE* **2004**, *5327*, 37–44.
(14) Cole, J. R.; Halas, N. J. *Appl. Phys. Lett.* **2006**, *89* (15).
(15) Charnay, C.; Lee, A.; Man, S. Q.; Moran, C. E.; Radloff, C.; Bradley, R. K.; Halas, N. J. *J. Phys. Chem. B* **2003**, *107* (30), 7327–7333.
(16) Xu, X.; Du, Q.; Peng, B.; Xiong, Q.; Hong, L.; Demir, H. V.; Wong, T. K. S.; Ko Kyaw, A. K.; Sun, X. W. *Appl. Phys. Lett.* **2014**, *105* (11), 113306.
(17) Mackey, M. A.; Ali, M. R. K.; Austin, L. A.; Near, R. D.; El-Sayed, M. A. *J. Phys. Chem. B* **2014**, *118* (5), 1319–1326.
(18) Dickerson, E. B.; Dreaden, E. C.; Huang, X. H.; El-Sayed, I. H.; Chu, H. H.; Pushpanketh, S.; McDonald, J. F.; El-Sayed, M. A. *Cancer Lett.* **2008**, *269*, 57.
(19) Zhang, L.; Xia, K.; Lu, Z.; Li, G.; Chen, J.; Deng, Y.; Li, S.; Zhou, F.; He, N. *Chem. Mater.* **2014**, *26* (5), 1794.
(20) Jia, H.; Fang, C.; Zhu, X. M.; Ruan, Q.; Wang, Y. X. J.; Wang, J. *Langmuir* **2015**, *31* (26), 7418.
(21) Pan, S. L.; Chen, M.; Li, H. L. *Colloids Surf., A* **2001**, *180* (1–2), 55.
(22) Sun, Y.; Xia, Y. *Science* **2002**, *298* (5601), 2176–2179.
(23) Mock, J. J.; Oldenburg, S. J.; Smith, D. R.; Schultz, D. A.; Schultz, S. *Nano Lett.* **2002**, *2* (5), 465–469.
(24) Loweth, C. J.; Caldwell, W. B.; Peng, X.; Alivisatos, A. P.; Schultz, P. G. *Angew. Chem. Int. Ed.* **1999**, *38* (12), 1808–1812.
(25) Li, Z.; Chung, S.-W.; Nam, J.-M.; Ginger, D. S.; Mirkin, C. A. *Angew. Chem. Int. Ed.* **2003**, *42* (20), 2306–2309.
(26) Yu, Y. Y.; Chang, S. S.; Lee, C. L.; Wang, C. R. C. *J. Phys. Chem. B* **1997**, *101* (34), 6661.
(27) Ghoreishi, S. M.; Behpour, M.; Khoobi, A. *Anal. Methods* **2012**, *4*, 2475.
(28) Huang, S.; Ma, H.; Zhang, X.; Yong, F.; Feng, X.; Pan, W.; Wang, X.; Wang, Y.; Chen, S. *J. Phys. Chem. B* **2005**, *109* (42), 19823–19830.
(29) Alekseeva, A. V.; Bogatyrev, V. A.; Khlebtsov, B. N.; Mel'nikov, A. G.; Dykman, L. A.; Khlebtsov, N. G. *Colloid J.* **2006**, *68* (6), 661–678.
(30) Zhu, J.; Yong, K. T.; Roy, I.; Hu, R.; Ding, H.; Zhao, L. L.; Swihart, M. T.; He, G. S.; Cui, Y. P.; Prasad, P. N. *Nanotechnology* **2010**, *21* (28).
(31) Nikoobakht, B.; El-Sayed, M. A. *Chem. Mater.* **2003**, *15* (10), 1957–1962.
(32) Chungang, W.; Tingting, W.; Zhanfang, M.; Zhongmin, S. *Nanotechnology* **2005**, *16* (11), 2555.
(33) Smith, D. K.; Korgel, B. A. *Langmuir* **2008**, *24* (3), 644–649.
(34) Ye, X.; Zheng, C.; Chen, J.; Gao, Y.; Murray, C. B. *Nano Lett.* **2013**, *13* (2), 765.
(35) Ye, X.; Gao, Y.; Chen, J.; Reifsnyder, D. C.; Zheng, C.; Murray, C. B. *Nano Lett.* **2013**, *13* (5), 2163.
(36) Koeppl, S.; Ghielmetti, N.; Caseri, W.; Spolenak, R. J. *Nanopart. Res.* **2013**, *15* (3), 1471.
(37) Johnson, C. J.; Murphy, C. J.; Dujardin, E.; Davis, S. A.; Mann, S. *J. Mater. Chem.* **2002**, *12* (6), 1765.
(38) Burrows, N. D.; Harvey, S.; Idesis, F. A.; Murphy, C. J. *Langmuir* **2016**.
(39) Murphy, C. J.; Sau, T. K.; Gole, A. M.; Orendorff, C. J.; Gao, J.; Gou, L.; Hunyadi, S. E.; Li, T. *J. Phys. Chem. B* **2005**, *109* (29), 13857–70.
(40) Alex, S. A.; Satija, J.; Khan, M. A.; Bhalerao, G. M.; Chakravarty, S.; Kasilingam, B.; Sivakumar, A.; Chandrasekaran, N.; Mukherjee, A. *Anal. Methods* **2015**, *7* (13), 5583–5592.
(41) Murphy, C. J.; Thompson, L. B.; Chernak, D. J.; Yang, J. A.; Sivapalan, S. T.; Boulos, S. P.; Huang, J.; Alkilany, A. M.; Sisco, P. N. *Curr. Opin. Colloid Interface Sci.* **2011**, *16* (2), 128.
(42) Zou, R.; Zhang, Q.; Zhao, Q.; Peng, F.; Wang, H.; Yu, H.; Yang, J. *Colloids Surf., A* **2010**, *372*, 5.
(43) Jana, N. R. *Small* **2005**, *1* (8–9), 875.
(44) Vigderman, L.; Zubarev, E. R. *Chem. Mater.* **2013**, *25* (8), 1450.
(45) Pérez-Juste, J.; Pastoriza-Santos, I.; Liz-Marzán, L. M.; Mulvaney, P. *Coord. Chem. Rev.* **2005**, *249* (17–18), 1870–1901.
(46) Ye, X.; Jin, L.; Caglayan, H.; Chen, J.; Xing, G.; Zheng, C.; Doan-Nguyen, V.; Kang, Y.; Engheta, N.; Kagan, C. R.; Murray, C. B. *ACS Nano* **2012**, *6* (3), 2804.
(47) Scarabelli, L.; Sánchez-Iglesias, A.; Pérez-Juste, J.; Liz-Marzán, L. M. *J. Phys. Chem. Lett.* **2015**, *6* (21), 4270.
(48) Scarabelli, L.; Grzelczak, M.; Liz-Marzán, L. M. *Chem. Mater.* **2013**, *25* (21), 4232.
(49) Jana, N. R.; Gearheart, L. A.; Murphy, C. J. *J. Phys. Chem. B* **2001**, *105* (19), 4065.
(50) Ratto, F.; Matteini, P.; Rossi, F.; Pini, R. J. *Nanopart. Res.* **2010**, *12* (6), 2029–2036.
(51) Gou, L.; Murphy, C. J. *Chem. Mater.* **2005**, *17* (14), 3668–3672.
(52) Jana, N. R.; Gearheart, L.; Murphy, C. J. *J. Phys. Chem. B* **2001**, *105*, 4065–4067.
(53) Lohse, S. E.; Murphy, C. J. *Chem. Mater.* **2013**, *25* (8), 1250.
(54) Wang, H.; Wu, Y.; Lassiter, B.; Nehl, C. L.; Hafner, J. H.; Nordlander, P.; Halas, N. J. *Proc. Natl. Acad. Sci. U.S.A.* **2006**, *103* (29), 10856–10860.
(55) Low, A.; Bansal, V. *Biomed. Imag. Interv. J.* **2010**, *6* (1), e9.
(56) Meena, S. K.; Celiksoy, S.; Schafer, P.; Henkel, A.; Sonnichsen, C.; Sulpizi, M. *Phys. Chem. Chem. Phys.* **2016**, *18* (19), 13246–13254.
(57) Chen, H. M.; Peng, H.-C.; Liu, R.-S.; Asakura, K.; Lee, C.-L.; Lee, J.-F.; Hu, S.-F. *J. Phys. Chem. B* **2005**, *109* (42), 19553–19555.
(58) Pérez-Juste, J.; Correa-Duarte, M. A.; Liz-Marzán, L. M. *Appl. Surf. Sci.* **2004**, *226* (1–3), 137–143.
(59) Link, S.; Mohamed, M. B.; El-Sayed, M. A. *J. Phys. Chem. B* **1999**, *103* (16), 3073.
(60) Huang, X.; Neretina, S.; El-Sayed, M. A. *Adv. Mater.* **2009**, *21* (48), 4880–4910.
(61) Sharma, V.; Park, K.; Srinivasarao, M. *Proc. Natl. Acad. Sci. U.S.A.* **2009**, *106* (13), 4981–4985.
(62) Akbulut, O.; Mace, C. R.; Martinez, R. V.; Kumar, A. A.; Nie, Z.; Patton, M. R.; Whitesides, G. M. *Nano Lett.* **2012**, *12* (8), 4060–4064.
(63) Park, K.; Koerner, H.; Vaia, R. A. *Nano Lett.* **2010**, *10* (4), 1433–1439.
(64) *NanoHybrids Make or Buy Gold Nanoparticles: A Quick Economic Analysis*. https://nanohybrids.net/pages/make-or-buy-gold-nanoparticles-a-quick-economic-analysis (accessed February 8, 2017).

Materials for Nanomaterial Synthesis

For a complete list of available materials, visit **SigmaAldrich.com/metalsalts**.

Gold

Name	Composition	Purity	Form	Prod. No.
Gold(III) bromide	$AuBr_3$	99.9% trace metals basis	powder	**398470-1G** **398470-5G**
Gold(I) chloride	AuCl	99.9% trace metals basis	powder	**481130-1G** **481130-5G**
Gold(III) chloride	$AuCl_3$	≥99.99% trace metals basis	solid	**379948-250MG** **379948-1G**
		99%	powder	**334049-500MG** **334049-5G**
Gold(III) chloride trihydrate	$HAuCl_4 \cdot 3H_2O$	≥99.9% trace metals basis	crystals and lumps	**520918-1G** **520918-5G** **520918-25G**
Gold(III) chloride hydrate	$HAuCl_4 \cdot xH_2O$	99.999% trace metals basis	crystals and lumps	**254169-500MG** **254169-5G**
		~52% Au basis	-	**50780-250MG** **50780-1G** **50780-5G**
		~50% Au basis	powder or crystals	**50790-250MG** **50790-1G** **50790-5G**
Gold(III) chloride solution	$HAuCl_4$	99.99% trace metals basis	liquid	**484385-10G** **484385-50G**
Gold(III) hydroxide	$Au(OH)_3$	-	powder	**398462-1G** **398462-5G**
Gold(I) iodide	AuI	99.9% trace metals basis	solid	**398411-1G**

Silver

Name	Composition	Purity	Form	Prod. No.
Silver carbonate	Ag_2CO_3	99.999% trace metals basis	powder	**438448-1G** **438448-10G**
		99%	powder and chunks	**179647-5G** **179647-25G** **179647-100G**
Silver chloride	AgCl	99.999% trace metals basis	powder and chunks	**204382-1G** **204382-5G** **204382-25G**
		99.998% trace metals basis	beads	**449571-1G** **449571-5G**
Silver chromate	Ag_2CrO_4	98%	powder	**227897-10G** **227897-50G**
Silver citrate hydrate	$AgO_2CCH_2C(OH)(CO_2Ag)CH_2CO_2Ag \cdot xH_2O$	-	powder	**361259-10G**
Silver cyanate	AgOCN	99%	powder and chunks	**244694-10G** **244694-50G**
Silver(I) fluoride	AgF	≥99.9% trace metals basis	powder	**226858-1G** **226858-5G** **226858-25G**
		99%	powder	**226866-5G** **226866-25G**
Silver(II) fluoride	AgF_2	≥98%	powder	**200921-10G**
Silver hexafluoroantimonate(V)	$AgSbF_6$	98%	powder	**227730-1G** **227730-5G** **227730-25G**
Silver hexafluorophosphate	$AgPF_6$	99.99% trace metals basis	powder	**450219-1G** **450219-5G**
Silver nitrate	$AgNO_3$	99.9999% trace metals basis	crystalline	**204390-1G** **204390-10G** **204390-50G** **204390-250G** **204390-2KG**
Silver nitrite	$AgNO_2$	99.98% trace metals basis	powder	**545015-5G** **545015-25G**
Silver perchlorate	$AgClO_4$	97%	solid	**674583-5G** **674583-25G**
Silver perchlorate hydrate	$AgClO_4 \cdot xH_2O$	99%	crystalline	**226548-5G** **226548-25G**
Silver(I) perrhenate	$AgReO_4$	99.99% trace metals basis	powder	**574198-1G**
Silver phosphate	Ag_3PO_4	98%	powder	**337382-25G**
Silver(I) sulfadiazine	$C_{10}H_9AgN_4O_2S$	98%	powder	**481181-5G** **481181-25G**
Silver sulfate	Ag_2SO_4	99.999% trace metals basis	powder or crystals	**204412-10G** **204412-50G**

Name	Composition	Purity	Form	Prod. No.
Silver tetrafluoroborate	$AgBF_4$	≥99.99% trace metals basis	powder	**483052-5G** **483052-25G**
Silver p-toluenesulfonate	$CH_3C_6H_4SO_3Ag$	≥99%	powder	**176427-10G** **176427-25G**

Cobalt

Name	Composition	Purity	Form	Prod. No.
Cobalt(II) bromide	$CoBr_2$	99.99% trace metals basis	beads	**427136-1G** **427136-5G**
		99%	powder	**334022-50G** **334022-250G**
Cobalt(II) chloride hydrate	$CoCl_2 \cdot xH_2O$	99.999% trace metals basis	powder and chunks	**203084-10G**
Cobalt(III) fluoride	CoF_3	-	powder	**236136-5G** **236136-25G** **236136-100G**
Cobalt(II) hydroxide	$Co(OH)_2$	95%	powder	**342440-250G**
Cobalt(II) iodide	CoI_2	99.999% trace metals basis	powder	**499129-1G**
Cobalt(II) nitrate hexahydrate	$Co(NO_3)_2 \cdot 6H_2O$	99.999% trace metals basis	crystals and lumps	**203106-10G** **203106-50G**
Cobalt(II) perchlorate hexahydrate	$Co(ClO_4)_2 \cdot 6H_2O$	-	crystals and lumps	**401404-25G**
Cobalt(II) tetrafluoroborate hexahydrate	$Co(BF_4)_2 \cdot 6H_2O$	99%	crystalline	**399957-25G**
Cobalt(II) thiocyanate	$Co(SCN)_2$	99.9% trace metals basis	powder	**497274-5G** **497274-25G**
		96%	powder	**216135-5G** **216135-25G** **216135-125G**
Hexaamminecobalt(III) chloride	$[Co(NH_3)_6]Cl_3$	99%	powder	**481521-25G** **481521-100G**
Pentaamminechlorocobalt(III) chloride	$[Co(NH_3)_5Cl]Cl_2$	98%	powder	**298301-10G**

Iridium

Name	Composition	Purity	Form	Prod. No.
Hydrogen hexachloroiridate(IV) hydrate	$H_2Cl_6Ir \cdot xH_2O$	99.98% trace metals basis	solid	**455962-1G**
		-	powder	**208973-1G** **208973-5G**
Iridium(III) bromide hydrate	$IrBr_3 \cdot xH_2O$	-	crystalline	**442119-1G**
Iridium(III) chloride	$IrCl_3$	99.8% trace metals basis	powder or crystals	**520721-1G**
		-	crystalline	**336807-500MG** **336807-2G**
Iridium(III) chloride hydrate	$IrCl_3 \cdot xH_2O$	99.9% trace metals basis	crystals and lumps	**203491-1G**
Iridium(IV) chloride hydrate	$IrCl_4 \cdot xH_2O$	≥99.9% trace metals basis	crystalline	**516996-1G**
		-	crystalline	**334480-500MG**
Pentaamminechloroiridium(III) chloride	$[Ir(NH_3)_5Cl]Cl_2$	99.95% trace metals basis	powder	**529281-1G**
Tetrairidium dodecacarbonyl	$Ir_4(CO)_{12}$	98%	powder	**299391-500MG**

Iron

Name	Composition	Purity	Form	Prod. No.
Iron(II) bromide	$FeBr_2$	99.999% trace metals basis	beads	**434000-1G**
Iron(III) bromide	$FeBr_3$	98%	powder	**217883-10G** **217883-50G**
Iron(II) chloride	$FeCl_2$	99.99% trace metals basis	beads	**450936-5G** **450936-25G**
		99.9% trace metals basis	beads	**450944-10G** **450944-50G**
Iron(II) chloride tetrahydrate	$FeCl_2 \cdot 4H_2O$	99.99% trace metals basis	crystals and lumps	**380024-5G** **380024-25G**
Iron(III) chloride	$FeCl_3$	≥99.99% trace metals basis	powder	**451649-1G** **451649-5G**
		≥99.9% trace metals basis	powder or crystals	**701122-1G** **701122-5G** **701122-25G**
Iron(III) citrate	$C_6H_5FeO_7$	-	powder	**F6129-250G** **F6129-1KG**
Iron(II) fluoride	FeF_2	98%	powder	**399841-10G**
Iron(III) fluoride	FeF_3	-	powder	**288659-10G**

Name	Composition	Purity	Form	Prod. No.
Iron(II) iodide	FeI_2	≥99.99% trace metals basis	beads	**400858-1G** **400858-10G**
Iron(III) nitrate nonahydrate	$Fe(NO_3)_3 \cdot 9H_2O$	≥99.999% trace metals basis	solid	**529303-25G**
Iron(II) oxalate dihydrate	$FeC_2O_4 \cdot 2H_2O$	99%	powder	**307726-25G** **307726-500G**
Iron(III) oxalate hexahydrate	$Fe_2(C_2O_4)_3 \cdot 6H_2O$	-	powder and chunks	**381446-5G** **381446-25G**
Iron(II) perchlorate hydrate	$Fe(ClO_4)_2 \cdot xH_2O$	98%	crystalline	**334081-5G** **334081-100G**
Iron(III) pyrophosphate	$Fe_4(P_2O_7)_3$	-	soluble crystals	**P6526-100G** **P6526-500G**
Iron(II) sulfate hydrate	$FeSO_4 \cdot xH_2O$	99.999% trace metals basis	solid	**450278-5G** **450278-25G**

Nickel

Name	Composition	Purity	Form	Prod. No.
Nickel(II) acetate tetrahydrate	$Ni(OCOCH_3)_2 \cdot 4H_2O$	≥99.0%, KT	powder or crystals	**72225-250G** **72225-1KG**
Nickel(II) bromide	$NiBr_2$	≥99.9% trace metals basis	powder	**561142-2G** **561142-10G**
		98%	solid	**217891-10G** **217891-50G**
Nickel(II) bromide hydrate	$NiBr_2 \cdot xH_2O$	98%	solid	**233730-25G**
Nickel(II) bromide ethylene glycol dimethyl ether complex	$NiBr_2 \cdot CH_3OCH_2CH_2OCH_3$	97%	powder	**406341-1G** **406341-5G**
Nickel(II) bromide 2-methoxyethyl ether complex	$NiBr_2 \cdot O(CH_2CH_2OCH_3)_2$	-	powder	**459674-5G**
Nickel carbonate, basic hydrate	$NiCO_3 \cdot 2Ni(OH)_2 \cdot xH_2O$	99.9% trace metals basis	powder	**544183-250G-A** **544183-1KG-A**
Nickel(II) carbonate hydroxide tetrahydrate	$2NiCO_3 \cdot 3Ni(OH)_2 \cdot 4H_2O$	-	powder	**339776-100G** **339776-500G**
Nickel(II) chloride	$NiCl_2$	99.99% trace metals basis	powder	**451193-5G** **451193-25G**
		98%	powder	**339350-50G** **339350-250G**
Nickel(II) chloride hexahydrate	$NiCl_2 \cdot 6H_2O$	99.999% trace metals basis	crystals and lumps	**203866-5G** **203866-25G**
		99.9% trace metals basis	solid	**654507-5G** **654507-25G** **654507-100G**
Nickel(II) chloride hydrate	$NiCl_2 \cdot xH_2O$	99.95% trace metals basis	solid	**364304-100G** **364304-500G**
Nickel(II) hydroxide	$Ni(OH)_2$	-	powder	**283622-250G** **283622-1KG**
Nickel(II) iodide	NiI_2	99.99% trace metals basis	powder	**466301-1G**
Nickel(II) nitrate hexahydrate	$Ni(NO_3)_2 \cdot 6H_2O$	99.999% trace metals basis	solid	**203874-20G** **203874-100G** **203874-500G**
Nickel(II) sulfamate tetrahydrate	$Ni(SO_3NH_2)_2 \cdot 4H_2O$	98%	solid	**262277-500G**
Nickel(II) sulfate	$NiSO_4$	99.99% trace metals basis	solid	**656895-10G** **656895-50G**
Nickel(II) sulfate heptahydrate	$NiSO_4 \cdot 7H_2O$	99.999% trace metals basis	crystals and lumps	**203890-10G** **203890-50G**

Platinum

Name	Composition	Purity	Form	Prod. No.
cis-Diamminetetrachloroplatinum(IV)	$Pt(NH_3)_2Cl_4$	99.9% trace metals basis	powder	**574759-1G**
trans-Diamminetetrachloroplatinum(IV)	$Pt(NH_3)_2Cl_4$	≥99.9% trace metals basis	powder	**574740-1G**
Hydrogen hexabromoplatinate(IV) hydrate	$H_2PtBr_6 \cdot xH_2O$	99.9% trace metals basis	powder and chunks	**398357-2G**
Hydrogen hexahydroxyplatinate(IV)	$H_2Pt(OH)_6$	99.9% trace metals basis	powder and chunks	**334472-500MG** **334472-2.5G**
Platinum(II) bromide	$PtBr_2$	98%	powder	**206121-1G**
Platinum(II) chloride	$PtCl_2$	99.99% trace metals basis	powder	**482315-1G**
		≥99.9% trace metals basis	powder	**520632-1G** **520632-5G**
Platinum(IV) chloride	$PtCl_4$	≥99.99% trace metals basis	powder and chunks	**379840-250MG** **379840-1G**
		≥99.9% trace metals basis	powder	**520640-1G** **520640-5G**
Platinum(II) cyanide	$Pt(CN)_2$	99.99% trace metals basis	solid	**442097-500MG**
Platinum(II) iodide	PtI_2	98%	powder	**206059-1G**

MilliporeSigma
3050 Spruce St.
Saint Louis, MO 63103

Sigma-Aldrich®
Lab Materials & Supplies

"...because innovative materials start with innovative chemistry."

Materials Matter

Your partner in materials innovation.

Find out more on SigmaAldrich.com/materials-synthesis

The life science business of Merck KGaA, Darmstadt, Germany operates as MilliporeSigma in the U.S. and Canada.

2017-03608
PB1036ENUS

MilliporeSigma